

An operator perturbation method for polarized line transfer

III. Applications to the Hanle effect in 1D media

K.N. Nagendra^{1,2}, H. Frisch¹, and M. Faurobert-Scholl¹

¹ Laboratoire G.D. Cassini (CNRS, UMR 6529), Observatoire de la Côte d'Azur, BP 4229, F-06304 Nice Cedex 4, France

² Indian Institute of Astrophysics, Bangalore 560034, India

Received 5 November 1997 / Accepted 17 December 1997

Abstract. In this paper we present an Approximate Lambda Iteration method to treat the Hanle effect (resonance scattering in the presence of a weak magnetic field) for lines formed with complete frequency redistribution. The Hanle effect is maximum in the line core and goes to zero in the line wings. Referred to as PALI-H, this method is an extension to non-axisymmetric radiative transfer problems of the PALI method presented in Faurobert-Scholl et al. (1997), hereafter referred to as Paper I. It makes use of a Fourier decomposition of the radiation field with respect to the azimuthal angle which is somewhat more general than the decomposition introduced in Faurobert-Scholl (1991, hereafter referred to as FS91).

The starting point of the method is a vector integral equation for a six-component source vector representing the non-axisymmetric polarized radiation field. As in Paper I, the Approximate Lambda operator is a block diagonal matrix. The convergence rate of the PALI-H method is independent of the polarization rate and hence of the strength and direction of the magnetic field. Also this method is more reliable than the perturbation method used in FS91.

The PALI-H method can handle any type of depth-dependent magnetic field. Here it is used to examine the dependence of the six-component source vector on the co-latitude, azimuthal angle and strength of the magnetic field. The dependence of the surface polarization on the direction of the line-of-sight and on the magnetic field is illustrated with polarization diagrams showing Q/I versus U/I at line center. The analysis of the results show that the full six-dimension problem can be approximated by a two-component modified resonance polarization problem, producing errors of at most 20 % on the surface polarization at line center.

Key words: polarization – magnetic fields – radiative transfer – scattering – stars: atmospheres – methods: numerical

1. Introduction

In Paper I of this series (Faurobert-Scholl et al. 1997), we have introduced an iterative numerical method of the Approximate Lambda Iteration (ALI) type to solve polarized radiative transfer equations describing the linear resonance polarization of spectral lines formed with complete frequency redistribution. The method described in Paper I can be applied to spectral lines formed in non-magnetic regions or in the presence of a weak isotropic turbulent magnetic field. It is tailored for radiation fields with an axial symmetry. The gain in memory space and computing time with respect to standard methods which do not make use of an Approximate Lambda Operator is quite significant.

Here we show that the method of Paper I can be generalized to handle the Hanle effect which describes the action of a weak magnetic field on resonance polarization. It applies when the magnetic sublevels of transition are sufficiently close in frequency that the natural linewidths of the sublevels overlap significantly. Permanent phase coherences between the Zeeman sublevels are partially destroyed leading to changes in the degree of linear polarization and in the orientation of the plane of polarization of the scattered radiation. The diagnostic potential of the Hanle effect with optically thick lines is already quite impressive. It was first used for solar prominences (Landi Degl'Innocenti et al. 1987; Bommier et al. 1989), then for the upper solar atmosphere (see the review in Faurobert-Scholl 1996). Other references can be found in Stenflo (1994). More recently the Hanle effect has been considered for the detection of weak magnetic fields in stellar envelopes (Ignace et al. 1997). Efforts to increase the efficiency of numerical methods able to treat this effect promise to be rewarding. The presence of an oriented magnetic field breaks the axial symmetry of the problem. The required generalization of the method of Paper I is achieved by means of an azimuthal Fourier expansion of the radiation field. As in Paper I we restrict ourselves to the approximation of complete frequency redistribution in the line.

In Sect. 2 we describe the polarized line transfer equations, and an azimuthal Fourier expansion method which can handle

any depth-dependent magnetic field. It is more general than the decomposition used in Faurobert-Scholl (1991), henceforth denoted by FS91, which was restricted to a magnetic field with constant azimuthal angle. In Sect. 3 we present a reduced radiative transfer problem for a six-dimensional vector radiation field. It is the starting point for the PALI-H operator perturbation method tested in Sect. 4 on a bench-marking problem with a uniform magnetic field. In Sect. 5 we study the effects of changing the direction and strength of a uniform vector magnetic field. A case of a vector magnetic field with a depth dependent azimuthal angle is also considered. We also discuss the basic symmetries of the problem. In Sect. 6 we apply the PALI-H method to construct various polarization diagrams. We study their dependence on the direction of the line of sight and on the vector magnetic field strength and orientation. We remark on a simple approximation to the full Hanle problem and show that it can be used for initial rough estimations of the magnetic field parameters in an inversion code for polarimetric observations. Some concluding remarks are presented in Sect. 7.

2. Basic equations

All the equations needed to calculate the Hanle effect produced by a depth-dependent magnetic field, for a line formed with complete frequency redistribution, are given in this section. They generalize equations obtained in FS91 for the case of a magnetic field with a uniform (constant with depth) azimuthal angle. Many of the equations to be given here have already been published, but are spread out in several articles, not all of them with easy access (such as Faurobert-Scholl 1993). Hence the presentation here of a complete set of equations.

2.1. Polarized line radiative transfer equation

In the presence of a weak magnetic field, the radiative transfer equation for the Stokes vector may be written as

$$\mu \frac{\partial \mathcal{I}(\tau, x, \mathbf{n})}{\partial \tau} = \phi(x) [\mathcal{I}(\tau, x, \mathbf{n}) - \mathcal{S}(\tau, x, \mathbf{n})], \quad (1)$$

where ϕ is the scalar absorption profile function (Landi Degl'Innocenti 1985). All the sign conventions, and the symbols for the physical quantities have the same meaning as in FS91: τ is the frequency averaged line optical depth, x is the frequency separation from line center, measured in Doppler width units, $\mathbf{n}(\theta, \varphi)$ is the propagation direction of the ray where θ is the co-latitude ($\mu = \cos \theta$) and φ is the azimuth of the ray. The positive optical depth is measured in the direction opposite to the vertical axis z (see Fig. 1). For lines formed with complete frequency redistribution, the vector source function \mathcal{S} is independent of frequency and may be written as

$$\mathcal{S}(\tau, \mathbf{n}) = (1 - \varepsilon) \int_{-\infty}^{+\infty} \phi(x') \int \hat{P}_H(\mathbf{n}, \mathbf{n}', \mathbf{B}) \mathcal{I}(\tau, x', \mathbf{n}') \frac{d\Omega'}{4\pi} dx' + \mathcal{S}^*(\tau), \quad (2)$$

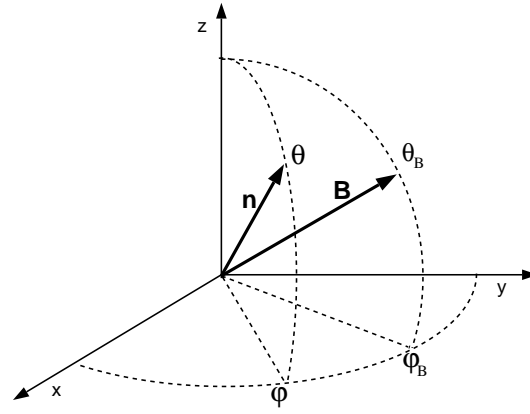


Fig. 1. Geometry specifying the direction of the magnetic field \mathbf{B} and of the line-of-sight \mathbf{n} . Angles θ and θ_B are the co-latitudes of \mathbf{n} and \mathbf{B} , respectively. The azimuthal angles φ and φ_B are measured starting from the x -axis in the anti-clockwise direction in the xy -plane

where \mathcal{S}^* is a given primary source term and \hat{P}_H is the Hanle phase matrix. In this paper all matrices are denoted with italic letters accentuated with a hat. As in FS91 and Landi Degl'Innocenti (1985), we neglect depolarizing collisions. The main results of this paper are independent of this simplifying assumption. Depolarizing collisions can be introduced by making ε a vector instead of scalar (Landi Degl'Innocenti et al. 1990).

The vector magnetic field \mathbf{B} is characterized by its strength B and by the angles θ_B and φ_B defined as shown in Fig. 1. The full Hanle phase matrix is a (4×4) matrix which couples together the three Stokes parameters I , Q and U but does not couple them to the Stokes parameter V . Here we are interested in the Hanle effect on the linear polarization of spectral lines. We may thus consider only the three-component Stokes vector $\mathcal{I} = (I, Q, U)^T$ and source vector $\mathcal{S} = (S_I, S_Q, S_U)^T$. The primary source term is assumed to be of thermal origin. Hence it is unpolarized and we may write it as $\mathcal{S}^*(\tau) = (S_I^*, 0, 0)^T$ where $S_I^* = \varepsilon B_\nu$, with B_ν the Planck function at the line center frequency. An explicit analytical expression of the Hanle phase matrix \hat{P}_H was first given by Landi Degl'Innocenti & Landi Degl'Innocenti (1988).

2.2. The azimuthal Fourier expansion method

In a 1D medium, in the absence of magnetic field and of incident collimated radiation, the radiation field is axially symmetric, i.e. it does not depend on the azimuth φ . This is no longer true when a magnetic field is present. It is well known that the non-axisymmetric transfer problem of Rayleigh scattering polarization can be simplified by expanding the azimuthal angle dependence of the specific intensity and source vector (see Chandrasekhar 1960 p. 250). This method is generalized for the Hanle scattering problem in FS91, where the azimuthal angle dependence of \mathcal{I} and \mathcal{S} is expanded in a Fourier series with respect to the azimuthal angle difference $\Delta\varphi = (\varphi - \varphi_B)$, where φ_B is assumed to be depth-independent. Here we present a more general formulation, where \mathcal{I} and \mathcal{S} are expanded in Fourier

series with respect to φ . It can thus be used in cases where φ_B varies with depth.

Because of its 2π -periodicity with respect to the variable φ , the specific intensity vector may be expanded as

$$\mathcal{I}(\tau, x, \mu, \varphi) = \sum_{k=-N}^{k=+N} \widetilde{\mathcal{I}}_k(\tau, x, \mu) e^{ik\varphi}, \quad (3)$$

where

$$\widetilde{\mathcal{I}}_k(\tau, x, \mu) = \int_0^{2\pi} \frac{d\varphi}{2\pi} \mathcal{I}(\tau, x, \mu, \varphi) e^{-ik\varphi}. \quad (4)$$

The Hanle phase matrix may be expanded in a two-dimensional Fourier expansion with respect to $\Delta\varphi = (\varphi - \varphi_B)$ and $\Delta\varphi' = (\varphi' - \varphi_B)$. In FS91 and Faurobert-Scholl (1993) it was shown that this expansion is limited to terms of order 2. Namely,

$$\begin{aligned} \hat{P}_H(\mu, \varphi, \mu', \varphi', \theta_B, \varphi_B, B) \\ = \sum_{k=-2}^2 \sum_{l=-2}^2 \hat{P}_H^{k,l}(\mu, \mu', \theta_B, B) e^{ik(\varphi - \varphi_B)} e^{il(\varphi' - \varphi_B)}. \end{aligned} \quad (5)$$

Explicit expressions of the Fourier coefficients were also given, however with some misprints.

2.3. Fourier coefficients of the Hanle phase matrix

The Fourier components $\hat{P}_H^{k,l}(\mu, \mu', \theta_B, B)$ may be written as linear combinations of matrices which depend only on the angular variables μ and μ' with scalar coefficients which depend only on the magnetic field variables θ_B and B . Namely,

$$\begin{aligned} \hat{P}_H^{k,l}(\mu, \mu', \theta_B, B) \\ = \sum_{m=1,4} \rho_m^{k,l}(\theta_B, B) \hat{p}_m^{k,l}(\mu, \mu'), \quad k, l = 0, \pm 1, \pm 2. \end{aligned} \quad (6)$$

In the particular case $k = l = 0$,

$$\hat{P}_H^{0,0}(\mu, \mu', \theta_B, B) = \hat{I}_{is} + \rho_1^{0,0} \hat{p}_1^{0,0}, \quad (7)$$

where \hat{I}_{is} is the isotropic matrix all the elements of which are zero except the element (1,1) which is unity. The coefficients $\rho_m^{k,l}$ are complex scalars whereas the matrices $\hat{p}_m^{k,l}$ have real elements.

A remarkable property of the Hanle phase matrix is that it has a diadic representation. It is of the same nature as the diadic representation for Rayleigh scattering introduced by Domke (1971; see also Ivanov 1995). The matrices $\hat{p}_m^{k,l}$ can be factorized as tensor products of two vectors depending on μ and μ' respectively and the isotropic matrix as the tensor product of two constant vectors. Furthermore, only six vectors \mathbf{Z}_i are necessary to construct the Hanle phase matrix. We indeed have

$$\hat{I}_{is} = \mathbf{Z}_0 \mathbf{Z}_0^T, \quad (8)$$

and

$$\hat{p}_m^{k,l}(\mu, \mu') = \mathbf{Z}_i(\mu) \mathbf{Z}_j^T(\mu'), \quad i, j = 1, \dots, 5. \quad (9)$$

Table 1. Values of the indices i and j for Eq. (9)

$k \setminus l$	m=1			m=2	
	0	1	2	1	2
0	1,1	1,2	1,3	1,4	1,5
1	2,1	2,2	2,3	2,4	2,5
2	3,1	3,2	3,3	3,4	3,5

$k \setminus l$	m=3			m=4	
	0	1	2	1	2
1	4,1	4,2	4,3	4,4	4,5
2	5,1	5,2	5,3	5,4	5,5

The index i depends on k and m and the index j on l, m . Table 1 shows how to obtain i and j for positive values of k and l . For example $\hat{p}_3^{2,1}(\mu, \mu') = \mathbf{Z}_5(\mu) \mathbf{Z}_2^T(\mu')$. The symmetry relations $\hat{p}_m^{k,l} = \hat{p}_m^{k,-l}$ and $\hat{p}_m^{k,l} = \hat{p}_m^{-k,l}$ provide the $\hat{p}_m^{k,l}$ for negative values of k and/or l .

The vectors \mathbf{Z}_i are given by :

$$\mathbf{Z}_0(\mu) = \begin{pmatrix} 1 \\ 0 \\ 0 \end{pmatrix}, \quad \mathbf{Z}_1(\mu) = \sqrt{\frac{W}{8}} \begin{pmatrix} 1 - 3\mu^2 \\ 3(1 - \mu^2) \\ 0 \end{pmatrix}, \quad (10)$$

$$\mathbf{Z}_2(\mu) = \frac{\sqrt{3W}}{2} \begin{pmatrix} \mu\sqrt{1 - \mu^2} \\ \mu\sqrt{1 - \mu^2} \\ 0 \end{pmatrix}, \quad (11)$$

$$\mathbf{Z}_3(\mu) = \frac{\sqrt{3W}}{4} \begin{pmatrix} 1 - \mu^2 \\ -(1 + \mu^2) \\ 0 \end{pmatrix}, \quad (12)$$

$$\mathbf{Z}_4(\mu) = \frac{\sqrt{3W}}{2} \begin{pmatrix} 0 \\ 0 \\ \sqrt{1 - \mu^2} \end{pmatrix}, \quad \mathbf{Z}_5(\mu) = \frac{\sqrt{3W}}{2} \begin{pmatrix} 0 \\ 0 \\ \mu \end{pmatrix}. \quad (13)$$

The parameter W is the standard $W_2(J, J')$ atomic depolarization factor which is equal to unity for a transition $J = 0, J' = 1$. Note that all the $\hat{p}_m^{k,l}$ are proportional to W .

The coefficients $\rho_m^{k,l}$, $k, l > 0$, may be written as

$$\rho_m^{k,l} = \frac{1}{4} [(a_m^{k,l} - a_m^{-k,-l}) - i(a_m^{k,-l} + a_m^{-k,l})], \quad (14)$$

$$\rho_m^{-k,l} = \frac{1}{4} [(a_m^{k,l} + a_m^{-k,-l}) - i(a_m^{k,-l} - a_m^{-k,l})], \quad (15)$$

$$\rho_m^{0,l} = \frac{1}{2} (a_m^{0,l} - i a_m^{0,-l}), \quad (16)$$

$$\rho_m^{k,0} = \frac{1}{2} (a_m^{k,0} - i a_m^{-k,0}), \quad (17)$$

$$\rho_m^{0,0} = a_m^{0,0}. \quad (18)$$

$$\rho_m^{-k,-l} = [\rho_m^{k,l}]^*, \quad \rho_m^{k,-l} = [\rho_m^{-k,l}]^*, \quad (19)$$

$$\rho_m^{0,-l} = [\rho_m^{0,l}]^*, \quad \rho_m^{-k,0} = [\rho_m^{k,0}]^*. \quad (20)$$

The notation $[]^*$ stands for complex conjugate.

Table 2. Symmetries of the coefficients $a^{k,l}$

$k \setminus l$	0	1	-1	2	-2
0	$a^{0,0}$	$a^{0,1}$	$a^{0,-1}$	$a^{0,2}$	$a^{0,-2}$
1	$a^{0,1}$	$a^{1,1}$	$a^{1,-1}$	$a^{1,2}$	$a^{1,-2}$
-1	$-a^{0,-1}$	$-a^{1,-1}$	$a^{-1,-1}$	$a^{-1,2}$	$a^{-1,-2}$
2	$a^{0,2}$	$a^{1,2}$	$-a^{-1,2}$	$a^{2,2}$	$a^{2,-2}$
-2	$-a^{0,-2}$	$-a^{1,-2}$	$a^{-1,-2}$	$-a^{2,-2}$	$a^{-2,-2}$

All the coefficients $a_m^{k,l}$, $m \geq 2$ can be expressed in terms of the $a_1^{k,l}$:

For $l \geq 0$ and all values of k :

$$a_2^{k,l} = (-1)^{l+1} a_1^{k,-l}, \quad a_2^{k,-l} = (-1)^l a_1^{k,l}. \quad (21)$$

For $k \geq 0$ and all values of l :

$$a_3^{k,l} = (-1)^{k+1} a_1^{-k,l}, \quad a_3^{-k,l} = (-1)^k a_1^{k,l}. \quad (22)$$

For $kl \geq 0$ (kl is the product of k by l):

$$a_4^{k,l} = (-1)^{|k|+|l|} a_1^{-k,-l}. \quad (23)$$

For $kl \leq 0$:

$$a_4^{k,l} = (-1)^{k+l+1} a_1^{-k,-l}. \quad (24)$$

The coefficients $a_1^{k,l}$ satisfy symmetry relations. For $l, k = \pm 1, \pm 2$:

$$\begin{aligned} a_1^{k,l} &= a_1^{l,k}, \quad \text{for } kl > 0, \\ a_1^{k,l} &= -a_1^{l,k}, \quad \text{for } kl < 0. \end{aligned} \quad (25)$$

For $k = 0$,

$$\begin{aligned} a_1^{0,l} &= a_1^{l,0}, \quad \text{for } l > 0, \\ a_1^{0,l} &= -a_1^{l,0}, \quad \text{for } l < 0. \end{aligned} \quad (26)$$

The symmetry relations satisfied by the $a_1^{k,l}$, which for simplicity are henceforth denoted by $a^{k,l}$, are also shown in Table 2. The $\rho_m^{k,l}$ depend thus only on 15 different coefficients which are given in Eq. (39).

2.4. Fourier expansion of the Stokes source vector \mathbf{S}

Substituting the azimuthal Fourier expansions of \hat{P}_H and \mathcal{I} in Eq. (2), we can perform analytically the azimuthal integration over φ' . This yields the azimuthal Fourier expansion of the source vector. As the Hanle phase matrix has no Fourier component of order higher than 2, the same property holds for the source vector. The complex Fourier components $\widetilde{\mathcal{I}}_k$ of the vector \mathcal{I} , defined as in Eq. (4), are given by

$$\begin{aligned} \widetilde{\mathcal{I}}_k(\tau, \mu) &= \delta_{k,0} \mathcal{I}^*(\tau) + (1 - \epsilon) e^{-ik\varphi_B} \frac{1}{2} \int_{-\infty}^{+\infty} dx' \phi(x') \\ &\int_{-1}^{+1} d\mu' \sum_{l=-2}^2 \hat{P}_H^{k,l}(\mu, \mu', \theta_B, B) e^{-il\varphi_B} \widetilde{\mathcal{I}}_{-l}(\tau, x', \mu'), \end{aligned} \quad (27)$$

where δ is the Kronecker symbol. Since we have an axially symmetric primary source term, only the Fourier component $k = 0$ has an inhomogeneous term. In the following we prefer to deal with real quantities (as in FS91). Boldface calligraphic uppercase letters accentuated with a tilde are used to denote the complex Fourier components. For the real Fourier components, we change the calligraphic font to an italic font and replace the tilde by an horizontal line. Boldface calligraphic uppercase letters are also used for the Stokes vector and associated source function.

The real Fourier components are given by

$$\begin{aligned} \overline{\mathbf{S}}_0 &= \widetilde{\mathcal{I}}_0, \\ \overline{\mathbf{S}}_k &= \widetilde{\mathcal{I}}_k + \widetilde{\mathcal{I}}_{-k}, \quad k > 0, \\ \overline{\mathbf{S}}_{-k} &= i(\widetilde{\mathcal{I}}_k - \widetilde{\mathcal{I}}_{-k}), \quad k > 0. \end{aligned} \quad (28)$$

The Fourier expansion of \mathcal{I} may then be written as

$$\begin{aligned} \mathcal{I}(\tau, \mu, \varphi) &= \overline{\mathbf{S}}_0(\tau, \mu) + \sum_{k=1}^{k=2} [\overline{\mathbf{S}}_k(\tau, \mu) \cos k\varphi \\ &+ \overline{\mathbf{S}}_{-k}(\tau, \mu) \sin k\varphi]. \end{aligned} \quad (29)$$

Each vector $\overline{\mathbf{S}}_k$ is a three-component vector. However for symmetry reasons, the azimuthal average of Stokes U vanishes. Thus $\overline{\mathbf{S}}_0$, which is the azimuthal average of \mathcal{I} , has only two components.

2.5. Factorization of the Fourier source vector

Following FS91, we introduce a new vector \mathbf{S}_F defined by

$$\mathbf{S}_F = [\overline{\mathbf{S}}_0, \overline{\mathbf{S}}_1, \overline{\mathbf{S}}_{-1}, \overline{\mathbf{S}}_2, \overline{\mathbf{S}}_{-2}]^T. \quad (30)$$

It is a 14-component vector since $\overline{\mathbf{S}}_0$ is a 2-component vector, while the other $\overline{\mathbf{S}}_{\pm k}$ are 3-component vectors. A 14-component vector denoted by \mathbf{I}_F is constructed in a similar fashion with the components of the real Fourier expansion coefficients $\overline{\mathbf{I}}_k$ of \mathcal{I} . It satisfies the radiative transfer equation:

$$\mu \frac{\partial \mathbf{I}_F(\tau, x, \mu)}{\partial \tau} = \phi(x) [\mathbf{I}_F(\tau, x, \mu) - \mathbf{S}_F(\tau, \mu)]. \quad (31)$$

Using Eqs. (7)–(28) and (30), it is straightforward, although lengthy, to show that \mathbf{S}_F can be written in the factorized form

$$\begin{aligned} \mathbf{S}_F(\tau, \mu) &= (1 - \epsilon) \hat{B}(\mu) \hat{R}(\varphi_B) \hat{M}_B(\theta_B, B) \hat{R}(-\varphi_B) \mathbf{J}(\tau) \\ &+ \hat{B}(\mu) \mathbf{S}^*(\tau). \end{aligned} \quad (32)$$

A key property of (32) is that $\mathbf{S}^*(\tau)$ and $\mathbf{J}(\tau)$ are six-component vectors. Hereafter all six-components vectors are denoted with boldface italic uppercase letters. The matrices and vectors appearing in this equation are defined in the following subsections.

2.5.1. The irreducible mean intensity \mathbf{J}

The vector \mathbf{J} is defined by

$$\mathbf{J}(\tau) = \frac{1}{2} \int_{-\infty}^{+\infty} \phi(x') \int_{-1}^{+1} [\hat{B}^T(\mu') \mathbf{I}_F(\tau, x', \mu')] d\mu' dx'. \quad (33)$$

It is directly related to the six irreducible tensors introduced by Landi Degl'Innocenti et al. (1990) in their density matrix formalism of the Hanle effect (see also Landi Degl'Innocenti 1984). The difference between the vector \mathbf{J} of this paper and the vector \mathbf{P} introduced in Paper I and in FS91 is that \mathbf{J} has no factor $(1 - \epsilon)$ and does not include the primary source term \mathcal{S}^* (see Eq. (14) in Paper I). It is a six-component vector while \mathbf{P} is a two-component vector. In analogy with Paper I, we denote the first two components of \mathbf{J} by J_1 and J_Q , whereas the other components are denoted by $J_{\pm 1}$ and $J_{\pm 2}$.

2.5.2. The matrices \hat{B}^T and \hat{B}

\hat{B}^T is a (6×14) matrix. In symbolic notation, it may be written as

$$\hat{B}^T(\mu) = \begin{pmatrix} \mathbf{Z}_0^T & 0 & 0 & 0 & 0 & 0 \\ \mathbf{Z}_1^T & 0 & 0 & 0 & 0 & 0 \\ 0 & \mathbf{Z}_2^T & -\mathbf{Z}_4^T & 0 & 0 & 0 \\ 0 & \mathbf{Z}_4^T & \mathbf{Z}_2^T & 0 & 0 & 0 \\ 0 & 0 & 0 & \mathbf{Z}_3^T & \mathbf{Z}_5^T & 0 \\ 0 & 0 & 0 & \mathbf{Z}_5^T & -\mathbf{Z}_3^T & 0 \end{pmatrix}. \quad (34)$$

To obtain the explicit expression it suffices to replace the line vectors \mathbf{Z}_i^T by their three components, except for \mathbf{Z}_0^T and \mathbf{Z}_1^T for which only the first two components are being used (the vectors $\mathbf{Z}_i(\mu)$ are given in Eqs. (10) to (13)). Because of the block structure of \hat{B}^T , the first two components of J_1 and J_Q of the vector \mathbf{J} depend only on the azimuthal average of \mathcal{I} (i.e. on $\overline{I_0}$), the third and fourth components $J_{\pm 1}$ depend only on the Fourier components $\overline{I_{\pm 1}}$ whereas the fifth and sixth components, $J_{\pm 2}$, depend only on $\overline{I_{\pm 2}}$.

\hat{B} is a (14×6) matrix which is the transpose of \hat{B}^T . In symbolic notation, it may be written as

$$\hat{B}(\mu) = \begin{pmatrix} \mathbf{Z}_0 & \mathbf{Z}_1 & 0 & 0 & 0 & 0 \\ 0 & 0 & \mathbf{Z}_2 & \mathbf{Z}_4 & 0 & 0 \\ 0 & 0 & -\mathbf{Z}_4 & \mathbf{Z}_2 & 0 & 0 \\ 0 & 0 & 0 & 0 & \mathbf{Z}_3 & \mathbf{Z}_5 \\ 0 & 0 & 0 & 0 & \mathbf{Z}_5 & -\mathbf{Z}_3 \end{pmatrix}. \quad (35)$$

Here the \mathbf{Z}_i are three-component column vectors, except for \mathbf{Z}_0 and \mathbf{Z}_1 which, as above, are two-component vectors. Clearly, $\hat{B}(\mu)$ is made of three blocks. The first (2×2) block, which contains the first two elements of the first row, is identical to the matrix $\hat{A}(\mu)$ of Paper I.

2.5.3. Primary source term

The second term in the r.h.s. of Eq. (32) is a primary source term. It comes from the first term in the r.h.s. of Eq. (27). It is easy to see that

$$\mathbf{S}^*(\tau) = S_I^*(\tau)[1, 0, 0, 0, 0, 0]^T, \quad (36)$$

and hence that $\mathbf{S}^*(\tau) = \hat{B}(\mu)\mathbf{S}^*(\tau)$. Being able to write the primary source term in this factorized form is necessary to arrive at the reduced problem described in Sect. 3. If the primary source term in Eq. (2) is not isotropic and unpolarized this factorization may not hold. A simple method for overcoming this difficulty is to write the Stokes vector as

$$\mathcal{I}(\tau, x, \mathbf{n}) = \mathcal{I}_d(\tau, x, \mathbf{n}) + \mathcal{I}^*(\tau, x, \mathbf{n}), \quad (37)$$

where $\mathcal{I}^*(\tau, x, \mathbf{n})$ is the solution of the problem with the internal source $\mathbf{S}^*(\tau)$ but no scattering term. A similar decomposition is used in Ivanov (1995) for Rayleigh scattering and in Ivanov et al. (1997) for resonance polarization. In the transfer equation for the diffuse radiation field $\mathcal{I}_d(\tau, x, \mathbf{n})$, the primary source term is then of the required form. When there are no internal primary sources but an external non-axisymmetric incident radiation field $\mathcal{I}_o(x, \mathbf{n})$, the same technique applies. It is now the directly transmitted field created by the incident radiation which should be subtracted from the total field.

2.5.4. The matrix \hat{M}_B

The (6×6) matrix \hat{M}_B depends only on the magnetic field strength B and its co-latitude θ_B . Except for the first row and the first column, it is almost the matrix of the coefficients $a_1^{k,l} = a^{k,l}$, $k, l = 0, \pm 1, \pm 2$. Taking into account the symmetries of the $a^{k,l}$ shown in Table 2, \hat{M}_B may be written as

$$\begin{pmatrix} 1 & 0 & 0 & 0 & 0 & 0 \\ 0 & M_{22} & M_{23} & M_{24} & M_{25} & M_{26} \\ 0 & 2M_{23} & M_{33} & M_{34} & M_{35} & M_{36} \\ 0 & -2M_{24} & -M_{34} & M_{44} & M_{45} & M_{46} \\ 0 & 2M_{25} & M_{35} & -M_{45} & M_{55} & M_{56} \\ 0 & -2M_{26} & -M_{36} & M_{46} & -M_{56} & M_{66} \end{pmatrix}, \quad (38)$$

where

$$\begin{aligned} M_{22} &= a^{0,0} = 1 - 3S_B^2 \frac{\gamma_B^2}{1 + \gamma_B^2} \left[1 - \frac{3\gamma_B^2}{1 + 4\gamma_B^2} S_B^2 \right], \\ M_{23} &= \frac{a^{0,1}}{2} = -\sqrt{\frac{3}{2}} C_B S_B \frac{\gamma_B^2}{1 + \gamma_B^2} \left[1 - \frac{6\gamma_B^2}{1 + 4\gamma_B^2} S_B^2 \right], \\ M_{24} &= \frac{a^{0,-1}}{2} = -\sqrt{\frac{3}{2}} S_B \frac{\gamma_B}{1 + \gamma_B^2} \left[1 - \frac{3\gamma_B^2}{1 + 4\gamma_B^2} S_B^2 \right], \\ M_{25} &= \frac{a^{0,2}}{2} = \sqrt{\frac{3}{2}} S_B^2 \frac{\gamma_B^2}{1 + 4\gamma_B^2} \left[1 - \frac{3\gamma_B^2}{1 + \gamma_B^2} C_B^2 \right], \\ M_{26} &= -\frac{a^{0,-2}}{2} = \sqrt{\frac{3}{2}} S_B^2 C_B \frac{3\gamma_B^3}{(1 + \gamma_B^2)(1 + 4\gamma_B^2)}, \\ M_{33} &= \frac{a^{1,1}}{2} = 1 - \frac{\gamma_B^2}{1 + \gamma_B^2} \left[1 - \frac{12\gamma_B^2}{1 + 4\gamma_B^2} S_B^2 C_B^2 \right], \\ M_{34} &= \frac{a^{1,-1}}{2} = -C_B \frac{\gamma_B}{1 + \gamma_B^2} \left[1 - \frac{6\gamma_B^2}{1 + 4\gamma_B^2} S_B^2 \right], \\ M_{35} &= \frac{a^{1,2}}{2} = C_B S_B \frac{3\gamma_B^2}{1 + 4\gamma_B^2} \left[1 - \frac{\gamma_B^2}{1 + \gamma_B^2} (C_B^2 - S_B^2) \right], \\ M_{36} &= -\frac{a^{1,-2}}{2} = -S_B \frac{\gamma_B}{1 + \gamma_B^2} \left[1 - \frac{6\gamma_B^2}{1 + 4\gamma_B^2} C_B^2 \right], \end{aligned}$$

$$\begin{aligned}
M_{44} &= \frac{a^{-1,-1}}{2} = 1 - \frac{\gamma_B^2}{1 + \gamma_B^2} \left[1 + \frac{3}{1 + 4\gamma_B^2} S_B^2 \right], \\
M_{45} &= \frac{a^{-1,2}}{2} = -S_B \frac{\gamma_B}{1 + 4\gamma_B^2} \left[1 - \frac{3\gamma_B^2}{1 + \gamma_B^2} C_B^2 \right], \\
M_{46} &= -\frac{a^{-1,-2}}{2} = -C_B S_B \frac{3\gamma_B^2}{(1 + \gamma_B^2)(1 + 4\gamma_B^2)}, \\
M_{55} &= \frac{a^{2,2}}{2} = 1 - \frac{\gamma_B^2}{1 + 4\gamma_B^2} \left[1 + 3C_B^2 \left(1 + \frac{\gamma_B^2}{1 + \gamma_B^2} S_B^2 \right) \right], \\
M_{56} &= -\frac{a^{2,-2}}{2} = C_B \frac{2\gamma_B}{1 + 4\gamma_B^2} \left[1 + \frac{3}{2} \frac{\gamma_B^2}{1 + \gamma_B^2} S_B^2 \right], \\
M_{66} &= \frac{a^{-2,-2}}{2} = 1 - \frac{\gamma_B^2}{1 + \gamma_B^2} \left[1 + \frac{3}{1 + 4\gamma_B^2} C_B^2 \right],
\end{aligned} \tag{39}$$

where

$$C_B = \cos \theta_B, \quad S_B = \sin \theta_B. \tag{40}$$

The dimensionless parameter γ_B , which depends on the intensity of the magnetic field, is given by

$$\gamma_B = \frac{2\pi\nu_L g_J}{A}, \tag{41}$$

where $\nu_L = eB/4\pi mc$ is the Larmor frequency of the electron in the magnetic field, g_J is the Landé factor of the upper level and A the destruction rate of the upper level alignment. It is the sum of the radiative, inelastic and depolarizing collision rates (see e.g. Bommier 1996, Eq. (32)). We note here that the matrix \hat{M}_B differs from the one in FS91. The elements M_{26} to M_{56} have opposite signs.

2.5.5. The matrix \hat{R}

The matrix \hat{R} may be written as

$$\hat{R}(\varphi_B) = \begin{pmatrix} 1 & 0 & 0 & 0 & 0 & 0 \\ 0 & 1 & 0 & 0 & 0 & 0 \\ 0 & 0 & c_1 & -s_1 & 0 & 0 \\ 0 & 0 & s_1 & c_1 & 0 & 0 \\ 0 & 0 & 0 & 0 & c_2 & s_2 \\ 0 & 0 & 0 & 0 & -s_2 & c_2 \end{pmatrix}, \tag{42}$$

where

$$c_1 = \cos \varphi_B, \quad s_1 = \sin \varphi_B, \tag{43}$$

$$c_2 = \cos 2\varphi_B, \quad s_2 = \sin 2\varphi_B. \tag{44}$$

The matrix $\hat{R}(-\varphi_B)$ comes from the factor $e^{-i\varphi_B}$ in Eq. (27) and $\hat{R}(\varphi_B)$ from $e^{-ik\varphi_B}$. This factor yields a rotation matrix which becomes $\hat{R}(\varphi_B)$ when it is commuted with $\hat{B}(\mu)$. The matrix $\hat{R}(\varphi_B)$ is a unitary matrix. It satisfies $\hat{R}(\varphi_B)^T = \hat{R}(-\varphi_B) = \hat{R}(\varphi_B)^{-1}$.

3. The irreducible transfer equation

The transfer equation (31) for the vector \mathbf{I}_F is simpler than the original transfer equation (1) for the Stokes vector \mathcal{S} , because

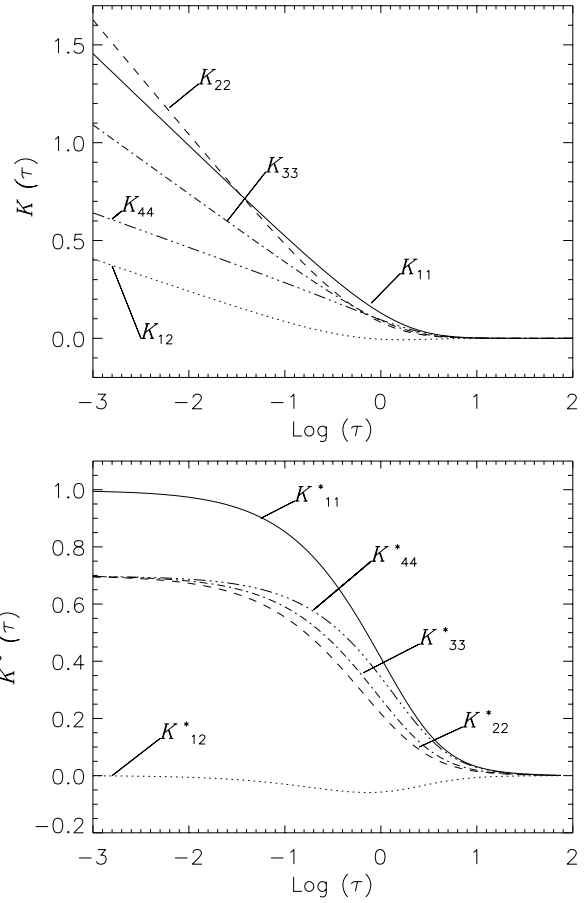


Fig. 2. The Hanle scattering kernels $K_{\alpha\beta}$ (upper panel) and their primitives $K_{\alpha\beta}^*$ (lower panel) in lin-log scales for Voigt profile with a damping parameter $a = 10^{-3}$ and $W = 1$. The normalization of $K_{\alpha\beta}$ is given by $K_{\alpha\beta}^*(\tau = 0) \simeq K_{\alpha\beta}(\tau = 10^{-3})$

the real Fourier components \overline{I}_k do not depend on the azimuth. However the source term \mathbf{S}_F is still a function of two variables: the optical depth τ , and the co-latitude θ of the ray. The factorization of \mathbf{S}_F , given in Eq. (32), suggests to introduce a new radiation field $\mathbf{I}(\tau, x, \mu)$, and a new source function $\mathbf{S}(\tau)$, that depends only on the optical depth, defined by:

$$\mathbf{I}_F(\tau, x, \mu) = \hat{B}(\mu) \mathbf{I}(\tau, x, \mu), \tag{45}$$

$$\mathbf{S}_F(\tau, \mu) = \hat{B}(\mu) \mathbf{S}(\tau). \tag{46}$$

We shall refer to the six-component vectors \mathbf{I} and \mathbf{S} as the “irreducible radiation field” and “irreducible source vector”. Eq. (32) shows that

$$\mathbf{S}(\tau) = (1 - \epsilon) \hat{H}_B(\theta_B, \varphi_B, B) \mathbf{J}(\tau) + \mathbf{S}^*(\tau), \tag{47}$$

where

$$\hat{H}_B(\theta_B, \varphi_B, B) = \hat{R}(\varphi_B) \hat{M}_B(\theta_B, B) \hat{R}(-\varphi_B). \tag{48}$$

When $B = 0$, the matrix \hat{M}_B becomes an unit matrix and so does \hat{H}_B . The vector \mathbf{S}^* has already been defined in Eq. (36).

Introducing Eq. (45) into Eq. (33), we can rewrite \mathbf{J} as

$$\mathbf{J}(\tau) = \frac{1}{2} \int_{-\infty}^{+\infty} \phi(x') \int_{-1}^{+1} \hat{B}^T(\mu') \hat{B}(\mu') \mathbf{I}(\tau, x', \mu') d\mu' dx'. \quad (49)$$

The irreducible radiation field satisfies the transfer equation

$$\mu \frac{\partial \mathbf{I}(\tau, x, \mu)}{\partial \tau} = \phi(x) [\mathbf{I}(\tau, x, \mu) - \mathbf{S}(\tau)]. \quad (50)$$

Left multiplying this equation on both sides by $\hat{B}(\mu)$ and commuting the matrix multiplication with the derivative with respect to τ , we indeed recover the transfer equation for \mathbf{I}_F .

We can now establish a vector integral equation for the irreducible source vector \mathbf{S} . It will be the basis for the iterative method presented in Sect. 4. Following the standard method, we first write the formal solution of Eq. (50). Using then Eqs. (47) and (49), we obtain :

$$\mathbf{S}(\tau) = (1 - \varepsilon) \hat{H}_B(\tau) \int_0^T \hat{K}(\tau - \tau') \mathbf{S}(\tau') d\tau' + \mathbf{S}^*(\tau), \quad (51)$$

where T is the optical thickness of the medium and $\hat{H}_B(\tau)$ the matrix defined in Eq. (48), the other three arguments being dropped for convenience.

The matrix \hat{K} is defined by

$$\hat{K}(\tau) = \frac{1}{2} \int_{-\infty}^{+\infty} \phi^2(x') \int_0^1 \hat{B}^T(\mu') \hat{B}(\mu') e^{-|\tau|\phi(x')/\mu'} \frac{d\mu'}{\mu'} dx'. \quad (52)$$

It is a (6×6) matrix which may be written as,

$$\begin{pmatrix} K_{11} & K_{12} & 0 & 0 & 0 & 0 \\ K_{12} & K_{22} & 0 & 0 & 0 & 0 \\ 0 & 0 & K_{33} & 0 & 0 & 0 \\ 0 & 0 & 0 & K_{33} & 0 & 0 \\ 0 & 0 & 0 & 0 & K_{44} & 0 \\ 0 & 0 & 0 & 0 & 0 & K_{44} \end{pmatrix}. \quad (53)$$

The first (2×2) block is identical to the kernel matrix for axisymmetric resonance polarization problems. The kernels K_{33} and K_{44} were introduced by Landi Degl'Innocenti et al. (1990). We recall that K_{11} is normalized to unity and K_{12} to zero. All the kernels K_{22} , K_{33} and K_{44} have the same normalization, viz.,

$$\int_{-\infty}^{+\infty} K_{\alpha\alpha}(\tau) d\tau = \frac{7}{10} W, \quad \alpha = 2, 3, 4. \quad (54)$$

The $K_{\alpha\beta}$ and their primitives $K_{\alpha\beta}^*$, defined by

$$K_{\alpha\beta}^*(\tau) = 2 \int_{\tau}^{\infty} K_{\alpha\beta}(u) du, \quad (55)$$

are shown in Fig. 2 for the case $W = 1$ and positive values of τ (remember that they are even functions of τ). The $K_{\alpha\beta}$ and their primitives are positive except for K_{12} and K_{12}^* . They decrease algebraically to zero at large optical depths and increase logarithmically as $\tau \rightarrow 0$. The properties of the propagating kernels K_{11} and K_{22} and of the mixing kernel K_{12} have been discussed at length in Paper I. The kernels K_{33} and K_{44} play a similar role as K_{22} .

To end this section we briefly comment on Eq. (51). It looks very much like the vector integral equation for resonance polarization in zero magnetic field considered in Paper I. However the true kernel of this integral equation is the product $\hat{H}_B \hat{K}$. When \hat{H}_B depends on optical depth, the integral equation is not of the Wiener-Hopf type since the kernel is not a displacement kernel. When \hat{H}_B is a constant matrix, the Wiener-Hopf character is maintained. However, in contrast with resonance polarization in zero magnetic field, the kernel is not a symmetric matrix and hence the transport operator is not self-adjoint. We stress also that in this equation all the components of \mathbf{S} are coupled in spite of the fact that the matrix \hat{K} has a very simple structure (see Eq. (53)).

For completeness we give below the analytical expressions of all the non-zero elements of \hat{K} :

$$K_{11}(\tau) = \frac{1}{2} \int_{-\infty}^{+\infty} \phi^2(x) E_1(|\tau|\phi(x)) dx, \quad (56)$$

$$K_{12}(\tau) = \frac{1}{2} \sqrt{\frac{W}{8}} \int_{-\infty}^{+\infty} \phi^2(x) [E_1(|\tau|\phi(x)) - 3E_3(|\tau|\phi(x))] dx, \quad (57)$$

$$K_{22}(\tau) = \frac{W}{8} \int_{-\infty}^{+\infty} \phi^2(x) [5E_1(|\tau|\phi(x)) - 12E_3(|\tau|\phi(x)) + 9E_5(|\tau|\phi(x))] dx, \quad (58)$$

$$K_{33}(\tau) = \frac{3W}{8} \int_{-\infty}^{+\infty} \phi^2(x) [E_1(|\tau|\phi(x)) + E_3(|\tau|\phi(x)) - 2E_5(|\tau|\phi(x))] dx, \quad (59)$$

$$K_{44}(\tau) = \frac{3W}{16} \int_{-\infty}^{+\infty} \phi^2(x) [E_1(|\tau|\phi(x)) + 2E_3(|\tau|\phi(x)) + E_5(|\tau|\phi(x))] dx. \quad (60)$$

The E_n are the usual exponential integral functions.

We note here for further use that \mathbf{J} also satisfies an integral equation. Combining Eqs. (51) with (47) we readily obtain

$$\mathbf{J}(\tau) = (1 - \varepsilon) \int_0^T \hat{K}(\tau - \tau') \hat{H}_B(\tau') \mathbf{J}(\tau') d\tau' + \mathbf{J}^*(\tau), \quad (61)$$

where

$$\mathbf{J}^*(\tau) = (1 - \varepsilon) \int_0^T \hat{K}(\tau - \tau') \mathbf{S}^*(\tau') d\tau'. \quad (62)$$

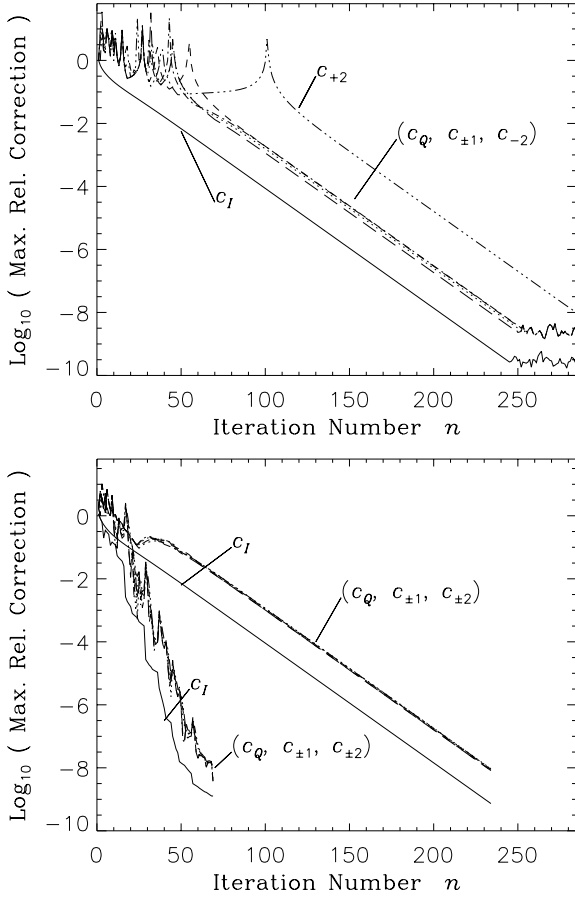


Fig. 3. Maximum relative corrections $c_\alpha^{(n)}$, $\alpha = I, Q, \pm 1, \pm 2$ as function of the iteration number n . Slab model with parameters $(T, a, \varepsilon, B_\nu) = (2 \cdot 10^9, 10^{-3}, 10^{-6}, 1)$, and $(\gamma_B, \theta_B, \varphi_B) = (1, 30^\circ, 0^\circ)$ is employed. The upper panel shows the $c_\alpha^{(n)}$ computed with the definition (66). The lower panel shows the same quantity computed with the modification given in Eq. (67). The effect of Ng acceleration is also shown in the lower panel. Note that all the curves (without Ng acceleration) have asymptotically the same slope for large values of n .

For a non-polarized primary source of thermal origin, $\mathbf{J}^* = (J_I^*, J_Q^*, 0, 0, 0, 0)$ with

$$J_I^*(\tau) = (1 - \varepsilon) S_I^* \left[1 - \frac{1}{2} [K_{11}^*(\tau) + K_{11}^*(T - \tau)] \right]. \quad (63)$$

J_Q^* is also given by Eq. (63) with K_{12}^* in place of K_{11}^* .

Thanks to the transformations carried out in the preceding sections, the calculation of the Stokes vector \mathcal{S} has been reduced to the solution of the vector transfer equation (50) where the vector source function \mathbf{S} depends only on optical depth and satisfies the integral equation (51). We solve it in the next section by an operator perturbation method.

4. The numerical method of solution

4.1. The iterative procedure

The integral equation for $\mathbf{S}(\tau)$ can be written in a symbolic form as

$$\mathbf{S} = (1 - \varepsilon) \hat{H}_B \hat{\Lambda} [\mathbf{S}] + \mathbf{S}^*. \quad (64)$$

After discretization of the τ -variable, the operator $\hat{\Lambda}$ becomes a $(N_T \times N_T)$ matrix, where N_T is the number of points in the optical depth grid $\{\tau_i\}$. Each element of $\hat{\Lambda}$ is a (6×6) matrix. Using the same kind of iterative method as in Paper I, we write the correction $\delta \mathbf{S}^{(n)}$ to the current estimate $\mathbf{S}^{(n)}$ as

$$\delta \mathbf{S}^{(n)} = [\hat{\mathbf{I}} - (1 - \varepsilon) \hat{H}_B \hat{\Lambda}^*]^{-1} [(1 - \varepsilon) \hat{H}_B \mathbf{J}^{(n)} - \mathbf{S}^{(n)} + \mathbf{S}^*]. \quad (65)$$

Here $\hat{\mathbf{I}}$ is the (6×6) identity matrix and $\hat{\Lambda}^*$ is the approximate $\hat{\Lambda}$ operator. To calculate $\mathbf{J}^{(n)}$ we solve the transfer equation (50) with $\mathbf{S}^{(n)}$ as source function and then average the resulting solution $\mathbf{I}^{(n)}$ over frequencies and directions according to Eq. (49). The operator $\hat{\Lambda}^*$ is constructed by keeping only the (6×6) matrices $\hat{\Lambda}(i, i)$, $i = 1, N_T$, on the diagonal of $\hat{\Lambda}$. Each matrix $\hat{\Lambda}(i, i)$ is calculated by placing a matrix point source (delta function source) at the grid point τ_i (see Paper I). Since this calculation has to be repeated at each grid point it turns out to be the most time consuming part of the iterative method.

4.2. Computational details and test problems

We consider isothermal, self-emitting plane parallel slab atmospheres with no incident radiation at the boundaries. These slab models are characterized by a set of input parameters $(T, a, \varepsilon, B_\nu)$, where T is the optical thickness of the slab, a the Voigt parameter of the line, ε the photon destruction probability per scattering, and B_ν the unpolarized internal thermal source. We consider the case of a pure line with no background continuum absorption. We restrict our attention to a two-level atom model with an atomic depolarization parameter set to unity ($W = 1$). The magnetic field is characterized by a set of 3 parameters $(\gamma_B, \theta_B, \varphi_B)$. For the optical depth grid, we use a resolution of 8 points per decade in a logarithmic scale, covering the range $10^{-2} \leq \tau \leq T$. A frequency grid with 2 points per decade in the value of the profile function ϕ is used. The last frequency point in the grid, x_{\max} , is chosen such that $T\phi(x_{\max}) < 10^{-2}$. A 5-point Gaussian quadrature formula with $\mu \in [0, 1]$ is employed for angular grid. The grid points $\{\mu_i\}$ correspond to the five angles $\theta = (18^\circ, 40^\circ, 60^\circ, 77^\circ, 87^\circ)$.

The calculations have been performed with two sets of atmospheric parameters:

- A first set $(T, a, \varepsilon, B_\nu) = (2 \cdot 10^9, 10^{-3}, 10^{-6}, 1)$. It corresponds to a line which has reached thermalization at mid-slab. This model is used to test the convergence of the iterative method.

- A second set $(T, a, \varepsilon, B_\nu) = (2 \cdot 10^2, 10^{-3}, 10^{-4}, 1)$. This model is used to study the influence of the magnetic field parameters on the polarization. At small optical depths (order of

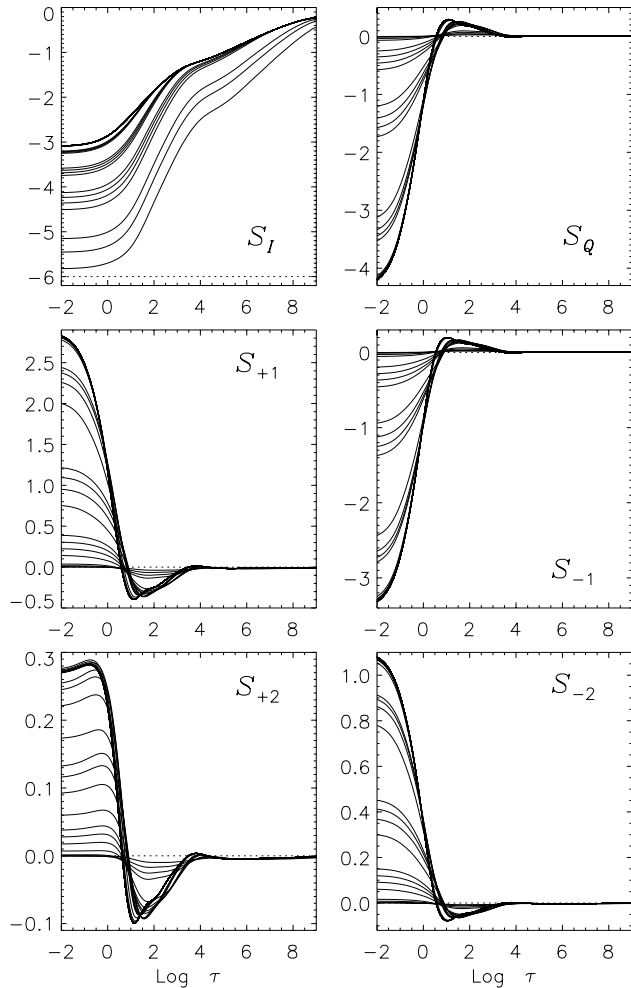


Fig. 4. Convergence history of the six components of $\mathbf{S}^{(n)}$ (see Eq. (47)). The upper left panel shows $\log_{10} S_I^{(n)}$ and the other panels $10^5 S_\alpha^{(n)}$, $\alpha = Q, \pm 1, \pm 2$. Same model as in Fig. 3. The dotted lines show the initial solutions (εB_ν for S_I , and zero for all other components). The effect of Ng acceleration (3-step jump of $S_\alpha^{(n)}$ towards convergence) is clearly seen. Since the slab is symmetric about the mid-plane, the results are shown only for the half-slab

unity or less), the qualitative behavior of the polarization is almost independent of the total optical thickness of the slab. It is of course computationally much faster to consider a slab with $T = 2 \cdot 10^2$ than a slab with $T = 2 \cdot 10^9$.

When the atmospheric and magnetic field parameters are uniform, the polarized radiation field is symmetric about the mid-plane at $T/2$. The transfer problem can be solved on a half-slab, by imposing as boundary condition at the mid-plane that the derivative of the intensity vector \mathcal{I} with respect to τ vanishes. The presence of a unidirectional magnetic field does not break the mid-plane symmetry, because of the symmetries of the Hanle phase matrix. For example $\mathcal{I}(0, x, \mu, \varphi) = \mathcal{I}(T, x, -\mu, \varphi)$.

4.3. Convergence properties of the method

As in Paper I, we have studied the convergence property of the method by following the dependence on the iteration number n of the $c_\alpha^{(n)}$, the maximum relative corrections of the components of the source vector \mathbf{S} . The upper panel in Fig. 3 shows the $c_\alpha^{(n)}$ defined by

$$c_\alpha^{(n)} = \max_{\tau_i} \left\{ \frac{|\delta S_\alpha^{(n)}(\tau_i)|}{|S_\alpha^{(n+1)}(\tau_i)|} \right\}, \quad (66)$$

with $|\delta S_\alpha^{(n)}(\tau_i)| = |S_\alpha^{(n+1)}(\tau_i) - S_\alpha^{(n)}(\tau_i)|$. The lower panel shows the $c_\alpha^{(n)}$ with the denominator in Eq. (66) replaced by

$$\bar{S}_\alpha^{(n+1)}(\tau_i) = \frac{1}{2} [|S_\alpha^{(n+1)}(\tau_i)| + |S_\alpha^{(n+1)}(\tau_{i+1})|]. \quad (67)$$

The iterative process is stopped when $\max_\alpha \{c_\alpha^{(n)}\} < 10^{-2} \varepsilon$. In the lower panel of Fig. 3 we also show the effect of an Ng acceleration applied only on $S_I(\tau)$ (see Paper I for details).

Comparing Fig. 3 of this paper with Figs. 4 and 5 of Paper I, we see that the convergence properties of the iterative method are exactly the same as in the non-magnetic case. This is a direct consequence of the fact that all the polarization components behave as slave modes of the intensity component in the asymptotic regime of large n . One can verify that the speed of convergence as measured by the ratio $c_1^{(n+1)}/c_1^{(n)}$ keeps the same value when a magnetic field is switched on. Thus a nice property of the PALI-H iterative method is that the convergence rate is independent of the strength and direction of the magnetic field.

Fig. 4 shows the convergence history of the six components of $\mathbf{S}^{(n)}$. The component S_I almost reaches its saturation value, $B_\nu = 1$, at mid-slab because the line is nearly thermalized. As a consequence $S_I(\tau) \simeq \sqrt{\varepsilon} = 10^{-3}$ at $\tau = 0$ and $\tau = T$. All the other components go to zero in the interior. Near the two boundaries they vary rapidly and change their sign.

To verify the accuracy and proper convergence of the iterative scheme we have compared its results with those of a non-iterative Feautrier scheme with a 8 points per decade resolution in spatial grid. Once the stopping criterion has been satisfied, the two solutions are identical up to 6 significant digits.

To estimate the optical depth grid-truncation error we have followed Auer et al. (1994) grid-doubling strategy. It has allowed us to estimate the errors on the intensity component S_I . Employing a 3-level grid doubling procedure with successively 2, 4 and 8 points per decade, we obtain on S_I , true errors of $4.54 \cdot 10^{-3}$ in the second stage, and $8.48 \cdot 10^{-4}$ in the third. For the polarization components, the grid-doubling strategy does not seem to offer a reliable estimation of the accuracy. More sophisticated methods seem to be required when dealing with functions which do not have a constant sign. We have also found that the grid-doubling strategy does not offer a significant gain in computing time for the reason that it is expensive to compute a (6×6) Hanle approximate operator on debut at each level of the grid doubling scheme. For resonance polarization with partial frequency redistribution this grid-doubling strategy appears on the contrary very promising (Paletou & Faurobert-Scholl 1997).

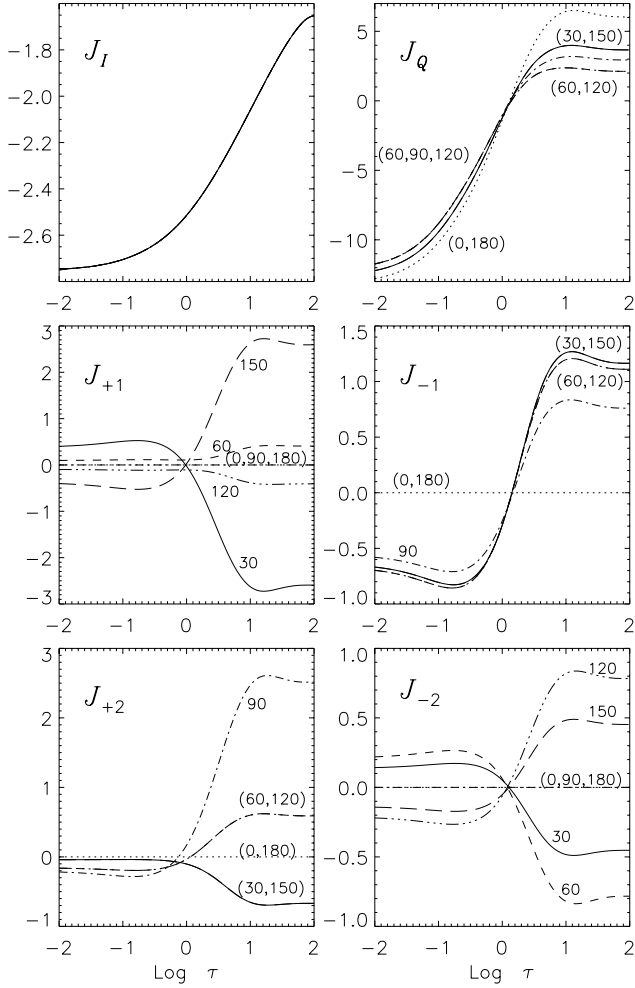


Fig. 5. Symmetries of the irreducible mean intensity vector components J_α with respect to the inclination angle θ_B of the magnetic field. The upper left panel shows $\log_{10} J_I$ and the other panels $10^5 J_\alpha$, $\alpha = Q, \pm 1, \pm 2$. Slab model with parameters $(T, a, \varepsilon, B_\nu) = (2 \cdot 10^2, 10^{-3}, 10^{-4}, 1)$ and $(\gamma_B, \varphi_B) = (1, 0^\circ)$. The numbers near the curves refer to the values of θ_B . Notice the symmetry/anti-symmetry of the polarized components about $\theta_B = 90^\circ$, the small sensitivity of J_Q to the value of θ_B and also the relative magnitudes of $J_{\pm 1}$ and $J_{\pm 2}$ in comparison with J_Q .

5. Properties of the irreducible vectors \mathbf{J} and \mathbf{S}

We discuss in this section the main properties of the six-component vectors \mathbf{J} and \mathbf{S} . We investigate in particular the dependence of \mathbf{J} and \mathbf{S} on the three parameters defining the magnetic field, θ_B , φ_B , and γ_B . In the results presented below, θ_B and γ_B are always kept uniform but we discuss one case with a depth-dependent φ_B since this feature could not be handled with the FS91 formulation. When φ_B is uniform, it is sufficient to calculate the solution with $\varphi_B = 0$. A simple transformation (see Sect. 5.4) yields the solution for an arbitrary φ_B .

All the results shown in this section have been obtained with the atmospheric parameters $(T, a, \varepsilon, B_\nu) = (2 \cdot 10^2, 10^{-3}, 10^{-4}, 1)$. For this slab model the product aT is

smaller than unity and hence the radiative transfer effects in the line are restricted to the Doppler core. We note also that the thickness T is much smaller than the thermalization length which is around $1/\varepsilon\sqrt{-\ln \varepsilon} \simeq 3 \cdot 10^3$. Hence the slab is effectively thin and the diffuse radiation field is almost independent of ε . Also because the line is not thermalized, the polarization goes to a constant at mid-slab. However, at depths around unity or less it behaves qualitatively as with the effectively thick slab model used in Sect. 4.

The integral equation (61) for \mathbf{J} and the relation (47) between \mathbf{J} and \mathbf{S} will be used in the analysis of the properties of \mathbf{J} and \mathbf{S} .

5.1. Dependence of \mathbf{J} on the co-latitude θ_B

For the computations in this section, we assume $\gamma_B = 1$ and let θ_B vary between 0° and 180° . As explained above, we have set the value of φ_B to zero. Fig. 5 shows the depth-dependence of the six components $J_I, J_Q, J_{\pm 1}, J_{\pm 2}$ for various values of θ_B . The upper left panel shows $\log_{10} J_I$ and the other panels $10^5 J_\alpha$, $\alpha = Q, \pm 1, \pm 2$. Figs. 7 to 10 devoted to \mathbf{S} also show $\log_{10} S_I$ in the upper left panel and $10^5 S_\alpha$, $\alpha = Q, \pm 1, \pm 2$, in the five other panels.

We list below the main properties of \mathbf{J} . Some of them have already been pointed out in the literature (see e.g. FS91 and the references therein).

- J_I is essentially independent of θ_B . Actually it is almost independent of the magnetic field as explained below.
- J_Q depends weakly on θ_B and is approximately equal to the resonance polarization value which corresponds to $\theta_B = 0$. Near the surface ($\tau \simeq 10^{-2}$), it is in absolute value about ten times smaller than J_I .
- In absolute value and near the surface, the components $J_{\pm 1}$ and $J_{\pm 2}$ are roughly ten times smaller than J_Q .
- All the polarization components J_α , $\alpha = Q, \pm 1, \pm 2$, change their sign at roughly the same optical depth τ .
- The components of \mathbf{J} satisfy the symmetry relations :

$$\begin{aligned} J_\alpha(\theta_B) &= J_\alpha(\pi - \theta_B), & \alpha &= I, Q, -1, +2, \\ J_\alpha(\theta_B) &= -J_\alpha(\pi - \theta_B), & \alpha &= +1, -2. \end{aligned} \quad (68)$$

These symmetries imply that $J_{+1} = J_{-2} = 0$ for $\theta_B = 90^\circ$. When $\theta_B = 0^\circ$ the components $J_{\pm 1}$ and $J_{\pm 2}$ are identically zero since the radiation field is axisymmetric.

The symmetries of \mathbf{J} are readily found by examining Eq. (61) with $\hat{H}_B = \hat{M}_B$ and the coefficients of the matrix \hat{M}_B given in Eq. (39). A change $\theta_B \rightarrow \pi - \theta_B$ amounts to change the sign of $C_B = \cos \theta_B$ while keeping $S_B = \sin \theta_B$ unchanged. Hence the coefficients $M_{23}, M_{26}, M_{34}, M_{35}, M_{46}, M_{56}$, which go to zero when $\theta_B = 90^\circ$, change sign under this transformation. One can then easily check that it leads to the symmetries presented in Eq. (68).

Consider now the structure of the matrix product $\hat{K}\hat{M}_B$. The first column is identical to the first column of \hat{K} . Therefore the components $J_{\pm 1}$ and $J_{\pm 2}$ are coupled to J_Q and between themselves but not to J_I . The component J_Q is coupled to J_I

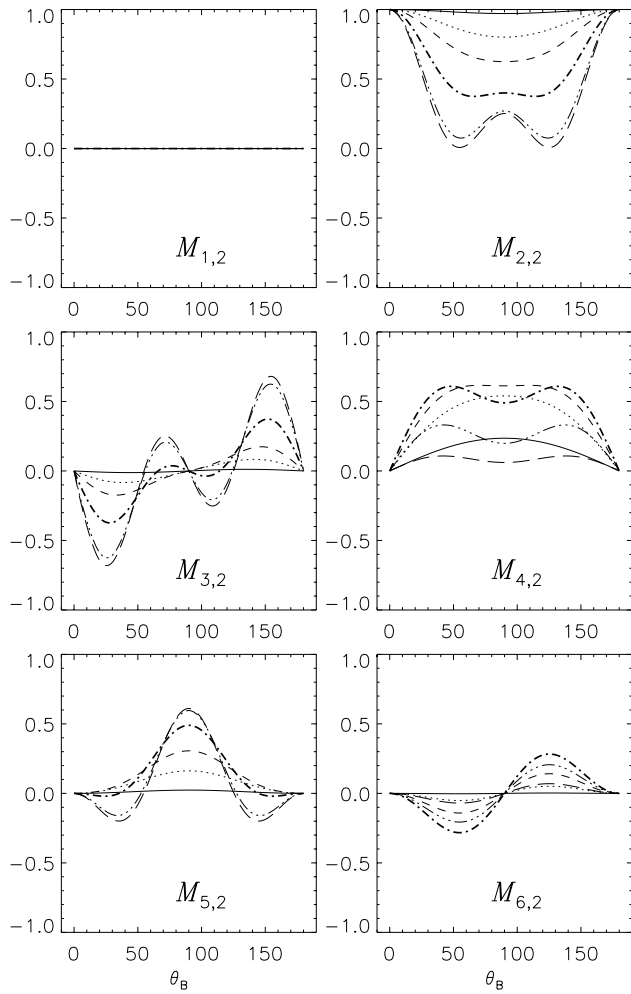


Fig. 6. Elements of the second column of the matrix $\hat{M}_B(\theta_B, B)$ as function of θ_B for various values of γ_B (i.e. of the magnetic field strength B). Solid lines: $\gamma_B=0.1$, dotted lines: $\gamma_B=0.3$, short-dashed lines: $\gamma_B=0.5$, dot-dashed lines: $\gamma_B=1$, triple-dot-dashed lines: $\gamma_B=3$, and long-dashed lines: $\gamma_B=10$. The case of $\gamma_B=1$ is highlighted for clarity. This figure is useful to understand the θ_B and γ_B dependence of the polarized source vector components S_{α} , shown in the Figs. 7 and 9

but this coupling is independent of the magnetic field and fairly weak, as already discussed in Paper I, because it is controlled by the kernel K_{12} . As for J_I , its dependence on the magnetic field is almost negligible since all the coupling terms with the polarization components, which are anyhow much smaller in magnitude, involve only the kernel K_{12} .

The optical depth at which J_Q and the other polarization components change sign is roughly determined by the optical depth at which the radiation field $I_1(\tau, x, \mu)$ corresponding to the source function $S_1(\tau)$ changes its angular dependence from limb darkening (at the surface) to limb brightening (in the interior). For this reason it is essentially independent of the magnetic field.

The values of J_I at the middle of the slab and at the surface can be evaluated with the scaling laws proposed in Frisch (1988)

for the Doppler profile. Correcting for a mistake in Eq. (4.6) of that paper, they may be written as

$$J_I\left(\frac{T}{2}\right) \sim \langle Q \rangle T\sqrt{\ln T},$$

$$J_I(0) \sim \langle Q \rangle T^{1/2}(\ln T)^{1/4}, \quad (69)$$

where $\langle Q \rangle$ is a mean value of the primary source term. For the model at hand, $\langle Q \rangle \simeq \epsilon B_\nu$. These scaling laws yield good estimates if one chooses $T = 10^2$ to evaluate J_I at the middle of the slab and $T = 2 \cdot 10^2$ to evaluate it at the surface. One gets $J_I(\frac{T}{2}) \sim 2 \cdot 10^{-2}$ and $J_I(0) \sim 2 \cdot 10^{-3}$. The exact numerical values are $J_I(\frac{T}{2}) = 2.24 \cdot 10^{-2}$ and $J_I(0) = 1.89 \cdot 10^{-3}$.

5.2. Dependence of \mathbf{S} on the co-latitude θ_B

In Fig. 7 we show the dependence of the six components of \mathbf{S} on θ_B . To obtain \mathbf{S} , it suffices to multiply \mathbf{J} by the matrix \hat{M}_B (or \hat{H}_B in the general case) (see Eq. (47)) and add the primary source term \mathbf{S}^* . For the model at hand \mathbf{S}^* can be neglected since it contributes only to the intensity component S_I and is at least an order of magnitude smaller than S_I (10^{-4} as compared to $2 \cdot 10^{-3}$ approximately; see Fig. 7). The main properties of the six components of \mathbf{S} are easy to explain. Because $J_{\pm 1}$ and $J_{\pm 2}$ are much smaller than J_Q and J_Q is much smaller than J_I , to evaluate the components of \mathbf{S} it is sufficient to keep the first and second column in the matrix \hat{M}_B written in Eq. (38). This approximation yields

$$S_I \simeq J_I, \quad S_Q \simeq M_{22}J_Q, \quad (70)$$

$$S_{+1} \simeq M_{32}J_Q, \quad S_{-1} \simeq M_{42}J_Q, \quad (71)$$

$$S_{+2} \simeq M_{52}J_Q, \quad S_{-2} \simeq M_{62}J_Q. \quad (72)$$

We show in Fig. 6 the elements of the second column of \hat{M}_B as function of θ_B for different values of γ_B . Note that they are of order unity, except for M_{12} which is identically zero. The approximations (70) to (72) explain why the polarization components of \mathbf{S} are of the same order of magnitude. Comparing Figs. 6 and 7 we see that the θ_B -dependence of the components of \mathbf{S} follows indeed closely the variation of the $M_{\alpha 2}$. We recall that J_Q is almost independent of θ_B (see Fig. 5). For example, near the surface, the decrease (in absolute value) of S_Q between $\theta_B = 0^\circ$ (resonance polarization) and $\theta_B = 60^\circ$ follows the decrease of the coefficient M_{22} . Then between 60° and 90° , M_{22} has a very small rise which also shows up in the variation of S_Q .

5.3. A perturbative method based on approximate solutions

The results discussed in this section suggest a perturbative method for solving the transfer problem and an approximation to evaluate the Stokes vector. The perturbation method was used in FS91. The approximation is also to be found in FS91. The idea is to keep only the first two columns in the matrix product $\hat{K}(\tau)\hat{M}_B$. The iterative method and the approximation have a common first step which is the calculation of $J_I(\tau)$ and $J_Q(\tau)$.

They are obtained by solving a modified resonance polarization problem with the kernel

$$\hat{K}(\tau) = \begin{pmatrix} K_{11} & M_{22}K_{12} \\ K_{12} & M_{22}K_{22} \end{pmatrix}. \quad (73)$$

A simple approximation for \mathbf{S} can then be set up by using the Eqs. (70) to (72). In comparison with full PALI-H code, the errors on the Stokes parameters for the line centre frequency ($x = 0$) are not very large (up to 20 %). In the line wings, they may reach a factor 2. They can be significantly reduced if one uses this first order approximation as starting solution for the iterative process described below. Just five perturbative steps are sufficient to bring them down to a fraction of a percent. In Sect. 6.6 we show the effect of this approximation on a polarization diagram.

To set up the iterative process, we must calculate the other harmonic components \mathbf{J}_α , $\alpha = \pm 1, \pm 2$. When only the first two columns of \hat{M}_B are kept, they are given by

$$J_\alpha(\tau) = (1 - \epsilon) \int_0^T K_\alpha(\tau - \tau') J_Q(\tau') d\tau', \quad (74)$$

with the kernel functions

$$K_{+1} = 2M_{23}K_{33}, \quad K_{-1} = -2M_{24}K_{33}, \quad (75)$$

$$K_{+2} = 2M_{25}K_{44}, \quad K_{-2} = -2M_{26}K_{44}. \quad (76)$$

These components are thus solutions of four scalar transfer equations with known source functions. The source function \mathbf{S} can then be obtained by applying Eq. (47) with the “full” \hat{H}_B (or \hat{M}_B) matrix. The solution of Eq. (50) combined with Eq. (49) yields a new value for \mathbf{J} and the process can be iterated.

It must be stressed that keeping only the first and second columns of the matrix $\hat{K}(\tau)\hat{M}_B$ may be insufficient when one of the coefficients M_{23} to M_{26} becomes close to zero because the self and the harmonic cross-coupling terms which have been neglected may then become the dominant ones. For $\theta_B = 60^\circ$, the coefficient $M_{32} = 2M_{23}$ is close to zero (see Fig. 6), therefore, the component J_{+1} will not be properly evaluated. Similarly, for $\theta_B = 30^\circ$, it is the component J_{+2} which will not be correctly evaluated. These errors are however of little importance, for polarization diagrams in particular, since they affect only the smallest component of \mathbf{J} , but they seem to generate convergence problems in the FS91 iterative method of solution. When comparing our PALI-H results with non-perturbative solutions and with the FS91 perturbative ones, we found some discrepancies with the latter solutions actually for the smallest of the components.

5.4. Dependence of \mathbf{S} on the azimuthal angle φ_B

We now let φ_B vary between 0 and 2π , assuming that φ_B is independent of the optical depth. As shown below, the dependence on φ_B is then very simple.

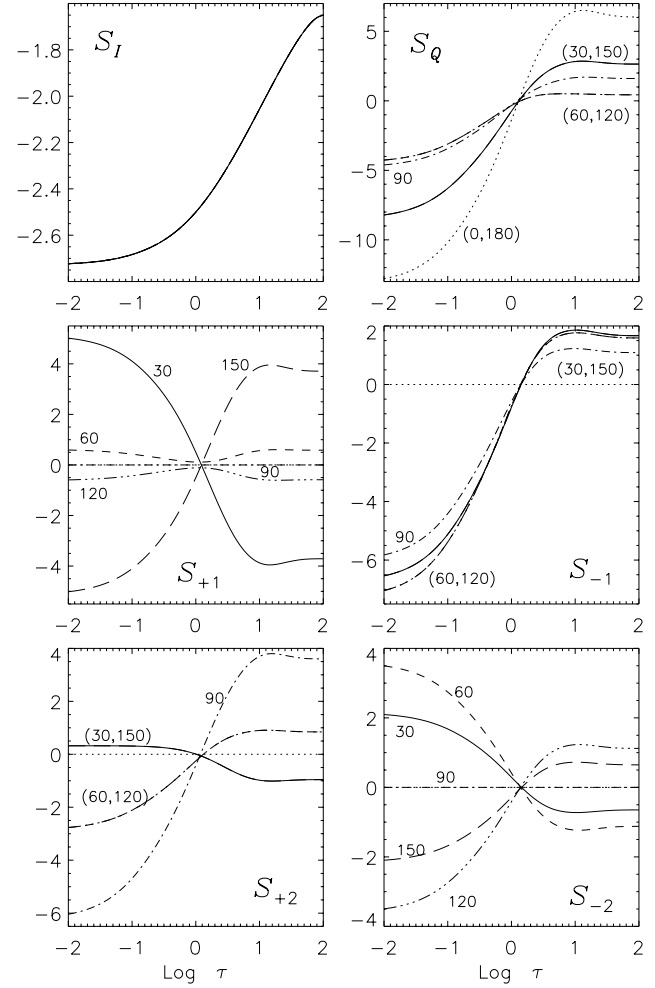


Fig. 7. Symmetries of the irreducible source vector components S_α with respect to θ_B . Same display and same atmospheric and magnetic parameters as in Fig. 5. The numbers near the curves refer to the values of θ_B . The Eq. (47) relates the components of source vector S_α to the components of mean intensity J_α , through the $\hat{M}_B(\theta_B, B)$ matrix. The dominant coupling originates from the elements of the second column $M_{\alpha 2}$, $\alpha = 2, 6$, which are plotted in Fig. 6

Eq. (61) and the factorization (48) suggest to introduce an auxiliary vector

$$\mathbf{J}^0(\tau) = \hat{R}(-\varphi_B)\mathbf{J}(\tau). \quad (77)$$

Using $\hat{R}(\varphi_B)\hat{R}(-\varphi_B) = \hat{1}$, with $\hat{1}$ the (6×6) identity matrix, and $\hat{R}(\varphi_B)\hat{K}(\tau)\hat{R}(-\varphi_B) = \hat{K}(\tau)$, it is easy to verify that \mathbf{J}^0 satisfies the integral equation (61) with \hat{H}_B replaced by \hat{M}_B . Hence \mathbf{J}^0 is independent of φ_B and is simply the reduced mean intensity vector for $\varphi_B = 0$. Eq. (77) yields

$$\mathbf{J}(\tau) = \hat{R}(\varphi_B)\mathbf{J}^0(\tau), \quad (78)$$

and

$$\mathbf{S}(\tau) = (1 - \epsilon)\hat{R}(\varphi_B)\hat{M}_B(\theta_B, B)\mathbf{J}^0(\tau) + S_I^*e. \quad (79)$$

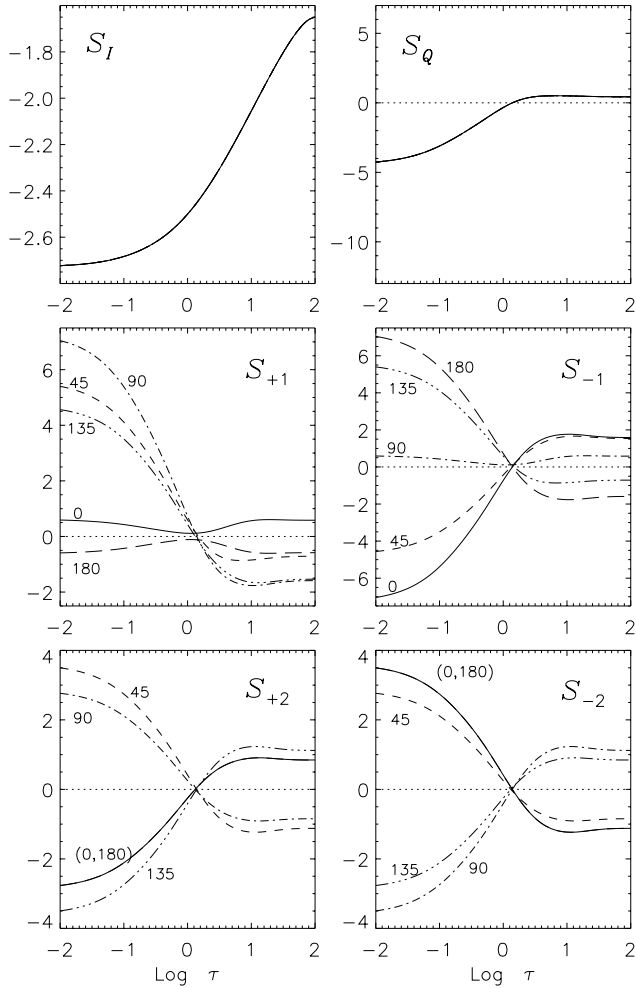


Fig. 8. Dependence of the irreducible source vector components $S_\alpha(\tau)$ on the magnetic field azimuth φ_B . Same display and same atmospheric parameters as in Fig. 5. Magnetic field parameters $(\gamma_B, \theta_B) = (1, 60^\circ)$. The numbers near the curves are the values of the azimuthal angle φ_B . The components S_I , and S_Q do not depend on φ_B . The dotted line is drawn only to indicate zero polarization

It is clear that Eqs. (78) and (79) could have been obtained directly by making a Fourier expansion of the Stokes vector \mathcal{S} in harmonics of $(\varphi - \varphi_B)$ as in FS91.

Fig. 8 shows the dependence on φ_B of the six components of \mathcal{S} for $\theta_B = 60^\circ$ and $\gamma_B = 1$. First we note that S_I and S_Q are independent of φ_B . The components $S_{\pm 1}(\tau)$ are 2π -periodic and change their sign under the transformation $\varphi_B \rightarrow (\pi + \varphi_B)$. The components $S_{\pm 2}(\tau)$ are π -periodic and change their sign under the transformation $\varphi_B \rightarrow (\pi/2 + \varphi_B)$. These properties are straightforward consequences of Eq. (79) and of the symmetry properties of $\hat{R}(\varphi_B)$ which can be read in Eq. (42).

5.5. Dependence of \mathcal{S} on the field strength parameter γ_B

We now assume that θ_B and φ_B are fixed, and let γ_B vary. Fig. 9 shows the dependence of the 6 components of \mathcal{S} on γ_B for $0 \leq \gamma_B < 3$. When $\gamma_B = 0$, only S_I and S_Q are different from

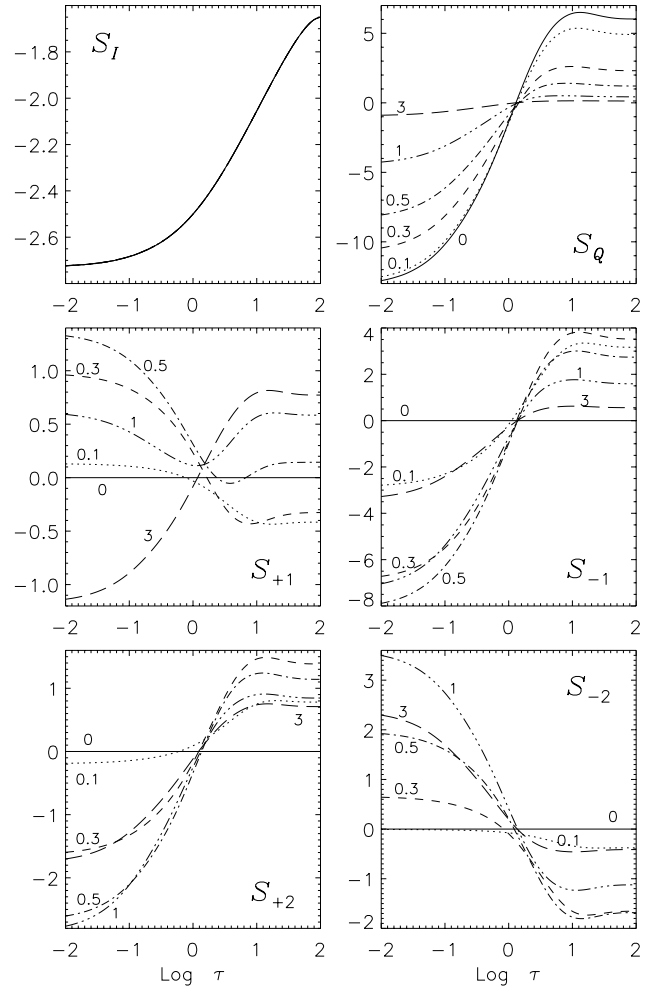


Fig. 9. Dependence of the irreducible source vector components S_α on the magnetic field strength parameter γ_B . Same display and same atmospheric parameters as in Fig. 5. Magnetic field parameters $(\theta_B, \varphi_B) = (60^\circ, 0^\circ)$. The numbers near the curves are the values of γ_B . The case $\gamma_B = 0$ refers to the non-magnetic resonance scattering polarization. At small optical depths, $S_{\pm 1}$ reach their maxima for $\gamma_B \simeq 0.5$, and $S_{\pm 2}$ do so for $\gamma_B \simeq 1.0$. Thus a narrow range $\gamma_B \sim 1$ represents the value of peak sensitivity of a line to the Hanle effect. The effects of γ_B on emergent polarization at line centre are shown in Fig. 15

zero because of the axial symmetry of the radiation field. For values of $\gamma_B > 3$, the Hanle effect saturates in the sense that, on further increase in γ_B , there is only a small change in the line polarization. Thus the range $0 < \gamma_B < 3$ represents the sensitivity range of the Hanle effect to the changes in magnetic field strength B .

The properties of \mathcal{S} can be analyzed exactly as in Sect. 5.1 with θ_B replaced γ_B . The dependence of J_I on γ_B is negligible and that of J_Q is fairly small (variation of 10% when γ_B increases from 0 to 3). According to the approximations (70) to (72) for \mathcal{S} , the γ_B -dependence of S_α is a direct mapping of the γ_B -dependence of the elements in the second column of the matrix $\hat{M}_B(\theta_B, B)$ (see Fig. 6 and Eq. (39)).

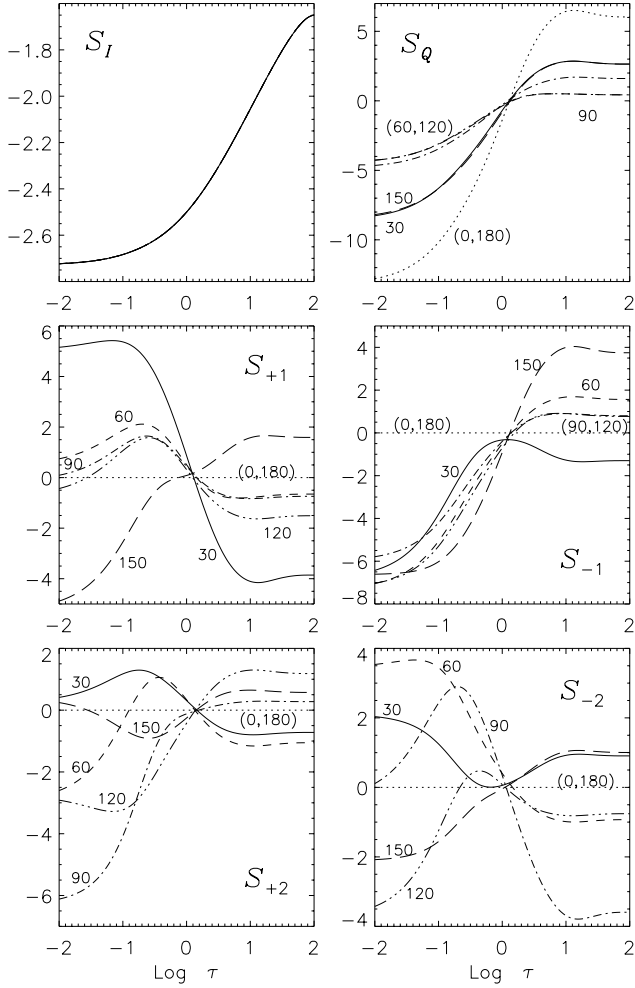


Fig. 10. The effect of a depth-dependent azimuth φ_B on the irreducible source vector components S_α . The depth-dependence of φ_B is given by Eq. (80). Same display and same atmospheric parameters as in Fig. 5. Magnetic field strength parameter $\gamma_B = 1$. The numbers near the curves are the values of θ_B . Compare this figure with the corresponding case of depth-independent azimuth shown in Fig. 7. Notice that the symmetries of S_α with respect to θ_B are broken by the depth-dependence of φ_B .

We can check on Fig. 9 that the dependence of S_I on γ_B is so weak that it cannot be detected on the graph. We see also that, for any θ_B , the surface value of S_Q monotonically approaches the zero level polarization, following indeed the monotonic decrease of M_{22} when γ_B increases. At the surface S_Q decreases by a factor of 3 when γ_B increases from 0 to 1. This is the well known Hanle depolarization effect.

For the other components the situation is more complex because of the non-monotonicity of other $M_{2\alpha}$. In the case of Fig. 9, the first harmonic components $S_{\pm 1}$ exhibit a ‘peak Hanle sensitivity’ around $\gamma_B = 0.5$, and the second harmonic components $S_{\pm 2}$ have their peak sensitivity for $\gamma_B \simeq 1$. By taking the limit $\gamma_B \rightarrow 0$ or $\gamma_B \rightarrow \infty$ in Eq. (39), one obtains that the source function is dominated by S_{-1} in the former case and by the two components S_{+1} and S_{+2} in the latter case.

5.6. The effect of a depth-dependent azimuth φ_B on S

In this section we assume that φ_B varies with optical depth according to

$$\varphi_B(\tau) = 45^\circ [(1 - e^{-5\tau}) - (1 - e^{-5\tau_1})], \quad (80)$$

where $\tau_1 = 10^{-2}$. This profile represents a strong exponential variation in the range of $0.1 < \tau < 1$. It gives $\varphi_B(\tau \sim 10^{-2}) = 0^\circ$ and $\varphi_B(\tau \sim 1) = 43^\circ$. With this model we must solve the transfer equation on the full slab, as there is no symmetry about the mid-plane.

Fig. 10 shows the components of S for several values of θ_B . This figure should be compared to Fig. 7. The approximation introduced in Sect. 5.3 can also be used here to analyze the results, provided that we replace the elements $M_{2\alpha}$ by the elements $H_{2\alpha}$ ($\alpha=Q, \pm 1, \pm 2$). As usual S_I is essentially independent of the magnetic field parameters. Since $H_{22} = M_{22}$, the component S_Q is almost insensitive to a variation of φ_B . For the other components, the most striking feature is the loss of symmetry with respect to their dependence on θ_B . In Sect. 6.3 we shall discuss the effect of a depth-dependent azimuthal angle on the emergent polarization.

6. The polarization diagrams

Useful tools for extracting magnetic field parameters from the observed Stokes parameters are plots of (Q/I) versus (U/I) . There are different ways of constructing them (see for instance Bommier et al. 1991; FS91; Stenflo 1994). They have been successfully used for the determination of weak magnetic fields in prominences and in the upper solar atmosphere (references can be found in Stenflo (1994) or Faurobert-Scholl (1996)). Throughout this paper, we show the polarization diagrams for depth $\tau = 0$, line center ($x = 0$), and selected values of μ . Each diagram is obtained by letting the radiation field azimuth φ (or the magnetic field azimuth φ_B when it is depth-independent) vary in the range $(0^\circ, 360^\circ)$. In practice, only Q and U are dependent on φ . For the resonance scattering problem ($\gamma_B = 0$), polarization is represented by a point on the $(U/I) = 0$ axis. For the Hanle effect ($\gamma_B \neq 0$), we get closed loops which are Lissajous curves since the azimuthal Fourier expansion of the radiation field is limited to second order terms.

These diagrams are easy to construct since Eqs. (29) and (45) and (46) allow us to explicitly express I , Q and U in terms of the 6 components of the irreducible intensity vector I . We thus find

$$I = I_I + \sqrt{\frac{W}{8}} (1 - 3\mu^2) I_Q + \frac{\sqrt{3W}}{2} \mu \sqrt{1 - \mu^2} [I_{+1} \cos \varphi + I_{-1} \sin \varphi] + \frac{\sqrt{3W}}{4} (1 - \mu^2) [I_{+2} \cos 2\varphi - I_{-2} \sin 2\varphi], \quad (81)$$

$$Q = \sqrt{\frac{W}{8}} 3(1 - \mu^2) I_Q +$$

$$\frac{\sqrt{3W}}{2} \mu \sqrt{1 - \mu^2} [I_{+1} \cos \varphi + I_{-1} \sin \varphi] - \frac{\sqrt{3W}}{4} (1 + \mu^2) [I_{+2} \cos 2\varphi - I_{-2} \sin 2\varphi]. \quad (82)$$

$$U = \frac{\sqrt{3W}}{2} \sqrt{1 - \mu^2} [I_{-1} \cos \varphi - I_{+1} \sin \varphi] + \frac{\sqrt{3W}}{2} \mu [I_{-2} \cos 2\varphi + I_{+2} \sin 2\varphi]. \quad (83)$$

The Stokes parameters depend on W through the factor \sqrt{W} but also through the components of \mathbf{I} since W enters in the expression of the kernel \hat{K} of the integral equation for \mathcal{S} (see Eqs. (50), (51), (56) to (60)). For optically thick lines, there is no simple dependence of U and Q on W . A simple scaling with W holds only for optically thin lines or when using the last scattering approximation as in Stenflo (1982). In these cases the components I_α , $\alpha=Q,\pm 1,\pm 2$ are proportional to \sqrt{W} .

We note here that we could have chosen the negative root of W when introducing the vectors \mathbf{Z}_i , $i = 1, \dots, 5$ (see Eqs. (9) to (13)). The components I_α , $\alpha=Q,\pm 1,\pm 2$, would have had opposite signs which would have compensated for the minus sign in front of \sqrt{W} .

Eq. (81) shows that Stokes I depends on all the six components of \mathbf{I} . The dominant contribution by far comes from the first term I_I , whatever the line of sight (LOS) and the magnetic field vector. Stokes Q depends on the last five components of \mathbf{I} . For small values of γ_B and a LOS close to the horizontal plane (μ small), the dominant contribution to Q comes from the term proportional to I_Q . Stokes U depends only on the last four components of \mathbf{I} . It is zero when the radiation field is axisymmetric. Equations (81) to (83) hold also for the components S_I, S_Q, S_U of the Stokes source vector \mathcal{S} provided the components of \mathbf{I} are replaced by the six irreducible source vector components ($S_I, S_Q, S_{\pm 1}, S_{\pm 2}$).

The polarization diagrams are generated as follows. We first solve the transfer equation for the axially symmetric irreducible intensity vector \mathbf{I} with our PALI-H transfer code. We then calculate $(I, Q, U)^T$ on a mesh of radiation field azimuths φ , using Eqs. (81) to (83). The points $((U/I), (Q/I))$ move in the anti-clockwise direction when φ is increased from 0° to 360° . When φ_B is constant, the polarization diagrams can be constructed by keeping φ constant and letting φ_B vary. Further, for CRD, Stokes Q and Stokes U show similar variation with frequency x : both have a single maxima at line centre and smoothly approach zero, or a constant value at the near wings ($x \sim 3$), depending on the values of ε and T (see Faurobert 1987; FS91). Hence, the polarization diagrams using the frequency averaged Stokes parameters exhibit similar shapes as the diagrams presented here for the line centre, except for a proportional decrease in the size of the diagrams, due to averaging. For all the polarization diagrams shown on Figs. 11-16, the slab model with the parameters $T = 2 \cdot 10^2$, $\varepsilon = 10^{-4}$, $a = 10^{-3}$ and $B_\nu = 1$ is used. Other parameters are noted in the figure captions, and on the figures.

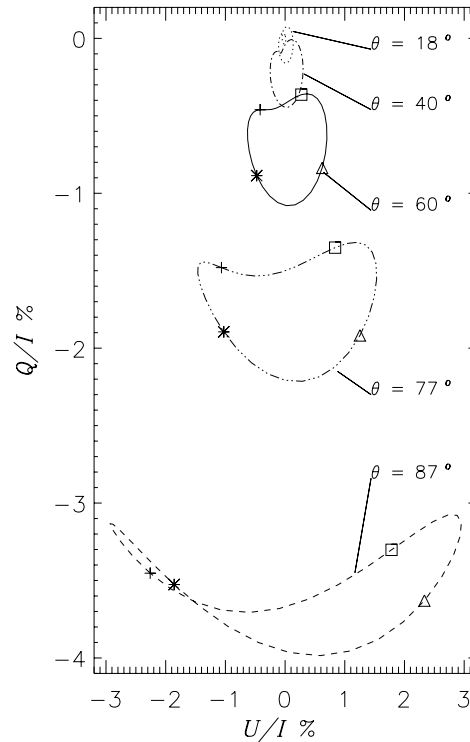


Fig. 11. θ -dependence of polarization diagrams at line centre. The numbers near the curves refer to the co-latitude θ of the LOS. The symbols on the curves correspond to different values of φ . The symbols: plus, asterisk, triangle and square correspond respectively to $\varphi = 0^\circ, 90^\circ, 180^\circ$ and 270° . Atmospheric parameters $(T, a, \varepsilon, B_\nu) = (2 \cdot 10^2, 10^{-3}, 10^{-4}, 1)$ and magnetic parameters $(\gamma_B, \theta_B, \varphi_B) = (1, 30^\circ, 0^\circ)$. Notice the expected limb-to-centre decrease in magnitude of the emergent linear polarization

6.1. Dependence on the radiation field co-latitude θ

In Fig. 11 we show the polarization diagrams for different values of θ . The magnetic field parameters are $(\gamma_B, \theta_B, \varphi_B) = (1, 30^\circ, 0^\circ)$. As θ varies from the tangential ($\theta = 87^\circ$) to the vertical direction ($\theta = 18^\circ$), the amplitude of variation of U decreases and so does the absolute value of Q . This leads to a decrease in the degree of linear polarization defined as $p = \sqrt{Q^2 + U^2}/I$. Note also the variation in the shape of the diagrams. It is due to the relative decrease of the first term in Eq. (82) with respect to the third one. In the extreme case of vertical LOS ($\mu = 1$), the polarization is non-zero, although it is very small as long as $\gamma_B \neq 0$ because of the contribution from the second harmonic in Q and U . This finite polarization in the vertical direction is known as ‘‘Hanle repolarization’’ (see Bomnier et al. 1991) because it is strictly zero when $\gamma_B = 0$. For $\varphi = 0^\circ$,

$$p(\theta = 0^\circ, \varphi = 0^\circ) = \frac{1}{2} \frac{\sqrt{3W(I_{+2}^2 + I_{-2}^2)}}{I_I - \sqrt{\frac{W}{2}} I_Q}. \quad (84)$$

We also note that for a given value of (Q/I) , there can be 2 or 4 possible values of (U/I) , and vice versa. Thus different

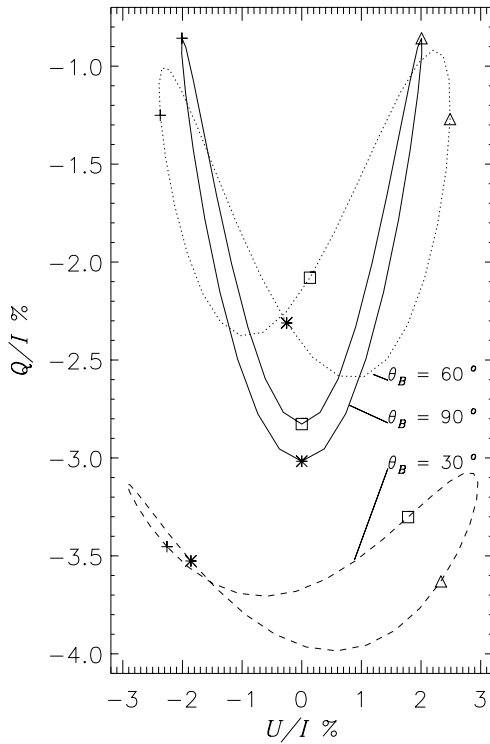


Fig. 12. θ_B -dependence of polarization diagrams at the line centre. The numbers near the curves refer to different co-latitudes θ_B of the magnetic field. Meaning of symbols and atmospheric parameters as in Fig. 11; magnetic field parameters $(\gamma_B, \varphi_B) = (1, 0^\circ)$. The co-latitude of the LOS is $\theta = 87^\circ$. Notice the symmetry of the diagram about $(U/I) = 0$ axis for the particular case $\theta_B = 90^\circ$

LOS or different values of φ_B may lead to the same degree of linear polarization and also the same angle of rotation of the plane of polarization $\chi = (1/2) \tan^{-1}(U/Q)$.

6.2. Dependence on the magnetic field co-latitude θ_B

In Fig. 12 we show the polarization diagrams for three different values of θ_B . The other two magnetic field parameters are held fixed: $(\gamma_B, \varphi_B) = (1, 0^\circ)$. The co-latitude of the LOS is $\theta = 87^\circ$. The values of θ_B are chosen between 0° and 90° . The diagrams for θ_B between 90° and 180° can be obtained by symmetry with respect to the axis $(U/I) = 0$. Indeed, when $\theta_B \rightarrow (\pi - \theta_B)$ and $\varphi \rightarrow (\pi - \varphi)$, Q does not change but U changes its sign. Hence, when $\theta_B = 90^\circ$, i.e. when the magnetic field vector is horizontal (see Fig. 1), the polarization diagrams are symmetric about the $(U/I) = 0$ axis. When the LOS is also in the horizontal plane the diagram becomes infinitely thin and looks like an open ended line.

6.3. Polarization diagram for a depth dependent azimuth $\varphi_B(\tau)$

In Fig. 13 we compare the polarization diagrams for the cases of constant azimuth ($\varphi_B = 0^\circ$), and a depth dependent azimuth $\varphi_B(\tau)$ given by Eq. (80). The other magnetic field parameters

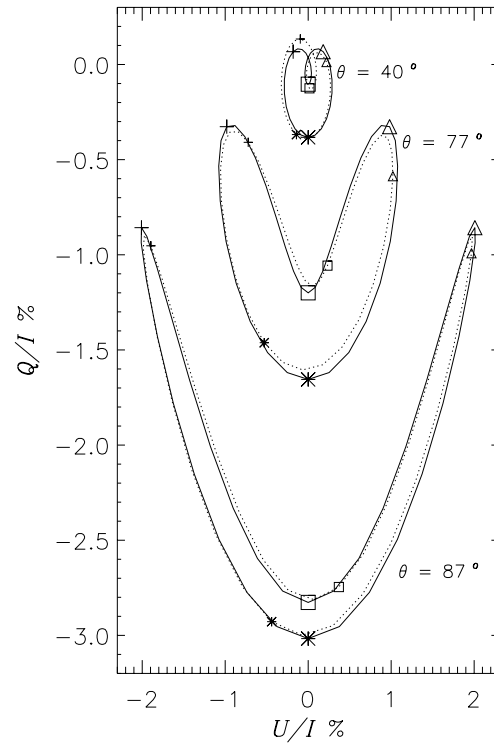


Fig. 13. Polarization diagrams at line center, for a uniform $\varphi_B (=0^\circ)$ and a depth dependent $\varphi_B(\tau)$ given by Eq. (80). Atmospheric parameters as in Fig. 11 and magnetic field parameters $(\gamma_B, \theta_B) = (1, 90^\circ)$. Constant azimuth: full lines with bigger symbols. Depth dependent azimuth: dotted lines with smaller symbols. The numbers near the curves refer to co-latitude θ of the LOS. Notice the loss of symmetry about the $(U/I) = 0$ axis when the magnetic field azimuth is depth dependent

are $(\gamma_B, \theta_B) = (1, 90^\circ)$. When $\varphi_B = 0^\circ$, the diagrams are symmetric about the $(U/I) = 0$ axis since we have chosen $\theta_B = 90^\circ$. This symmetry is broken by a depth dependent $\varphi_B(\tau)$. Fig. 13 shows clearly, that the polarization diagrams are almost insensitive to the $\varphi_B(\tau)$ law used in our model. The sensitivity to the depth variation of $\varphi_B(\tau)$ strongly depends on the gradient of $\varphi_B(\tau)$ in the region of formation of the line core. We have noticed that the effects of a variable φ_B can become significant with a variation $\Delta\varphi_B(\tau)$ of 90° or more within narrow layers near the surface of the slab ($\tau \ll 1$). The diagrams become very asymmetric about the $(U/I) = 0$ axis, and reduce drastically in size. So unless one has good reasons to suspect a strong variation of $\varphi_B(\tau)$ within the line core formation region, assuming a uniform $\varphi_B(\tau)$ is a reasonable hypothesis, in modelling efforts.

6.4. Dependence on the magnetic field strength parameter γ_B

In Fig. 14 we present the polarization diagrams for different values of γ_B , the strength parameter of the magnetic field. The field direction is fixed at $(\theta_B, \varphi_B) = (60^\circ, 0^\circ)$. The models are the same as those used for Fig. 9. The co-latitude of the LOS is 87° . The non-magnetic resonance scattering polarization ($\gamma_B = 0$) yields the point $(U/I) = 0$, $(Q/I) = -5.61\%$. For small values

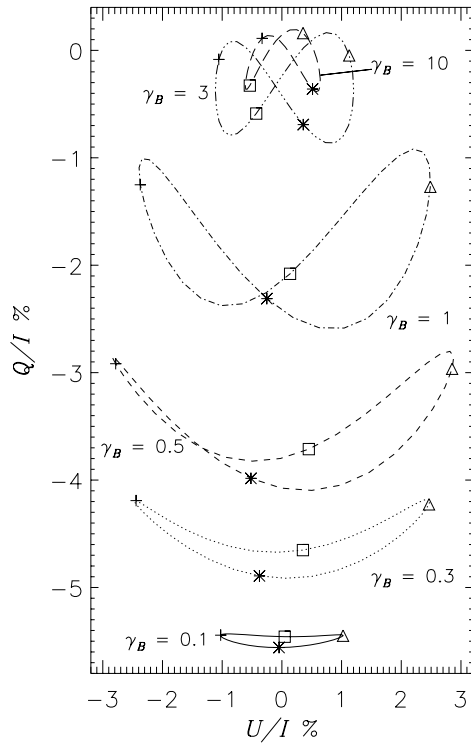


Fig. 14. The effect of magnetic field strength on the polarization diagrams at line center and $\theta = 87^\circ$ of the LOS. Meaning of symbols and atmospheric parameters as in Fig. 11; magnetic field parameters $(\theta_B, \varphi_B) = (60^\circ, 0^\circ)$. The different values of γ_B are indicated near the diagrams. Notice the strong increase in U/I between $\gamma_B = 0.1$ and $\gamma_B = 0.3$ and the saturation of the depolarizing efficiency for large values of γ_B

of γ_B (~ 0.1), the component I_Q is the dominant one (see Fig. 9), hence U is small and the diagrams are quite flat. When $\gamma_B \sim 1$, the last five components are more or less of the same order, which explains the butterfly shape of the diagrams. Fig. 14 also shows clearly that for large values of γ_B ($\gg 3$), the Hanle effect becomes negligible.

6.5. The two-parameter polarization diagrams

As suggested in Bommier et al. (1991), the determination of magnetic field parameters from observational data can be attempted with the help of two-parameter diagrams showing a network of iso-strength and iso-azimuth curves. For a given LOS, determined by the values of θ and φ , one chooses a value of θ_B and vary the two other parameters of the magnetic field, γ_B and φ_B . Then in the plots of Q/I versus U/I , one draws not only the iso-strength curves as in Fig. 14 but also the iso-azimuth curves. Fig. 15 shows such a diagram for a LOS with $\theta = 90^\circ$ and $\varphi = 0^\circ$ and a magnetic field with $\theta_B = 90^\circ$. To draw this figure we have used the slab model ($T = 2 \cdot 10^2$) and varied γ_B in the range 0–100. Similar two-parameter diagrams for different choices of θ and θ_B are shown in Bommier et al. (1991).

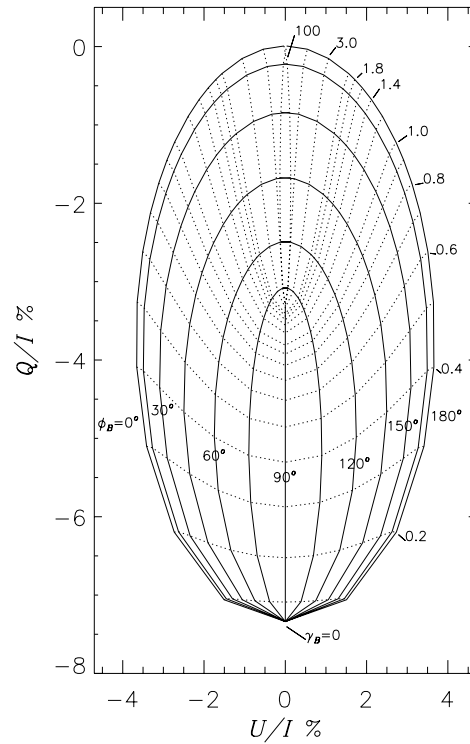


Fig. 15. The two-parameter polarization diagrams for Hanle effect. Same atmospheric parameters as in Fig. 11. Magnetic field parameters $\theta_B = 90^\circ$, γ_B in the range (0–100) and φ_B in the range (0–180°). The iso-strength curves (solid lines) are drawn by fixing φ_B and varying γ_B . The iso-strength curves (dotted lines) are drawn by fixing γ_B and varying φ_B . All the curves in the figure are symmetric about the $(U/I) = 0$ axis. The LOS is fixed at $(\theta, \varphi) = (90^\circ, 0^\circ)$. The results are presented for the line centre. The iso-strength curves show the Hanle depolarization and saturation effects clearly. The iso-azimuth curves show the effect of rotation of the plane of polarization when γ_B varies

When both the LOS and the magnetic field are lying in the horizontal plane, as in Fig. 15, the iso-strength loops become infinitely thin and look like open ended curves. Also it is sufficient to let φ_B vary in the range 0–180° to cover a whole iso-strength curve (dotted line). When γ_B is small the iso-strength curves are almost horizontal for the reason given in Sect. 6.4. When γ_B is large the two prongs of the curve become almost vertical. When $\gamma_B \rightarrow \infty$, the ordinate of the lowest point reaches a limiting value given by $Q/I = (3/2\sqrt{2})\sqrt{W}I_Q/I$.

The iso-azimuth curves (solid lines) are open ended lines which start at $\gamma_B = 0$ and end at $\gamma_B = 100$. All the iso-azimuth curves merge at the point $\gamma_B = 0$ where $U/I = 0$ and $Q/I = -7.4\%$. The iso-azimuth curves for $\varphi_B = 90^\circ$ (and $\varphi_B = 270^\circ$) are straight lines which coincide with the $U/I = 0$ axis.

When an observational data point $(U/I, Q/I)$ falls within an approximate interval defined by $[\Delta\gamma_B, \Delta\varphi_B]$, we get upper and lower limits on the possible values of γ_B and φ_B , which may further be used for modelling. This approach is reasonable when an independent estimate of θ_B is available. It is worthwhile to note that in order to construct a series of such two-parameter

polarization diagrams corresponding to different values of the fixed magnetic field parameter, a fast method for the computation of emergent Stokes parameters is required. The approximation introduced in Sect. 5.3 can serve that purpose.

6.6. A fast method of generating the polarization diagrams

The method is very simple. One first solves a two-component polarized transfer problem with the kernel given in Eq. (73) to calculate J_I and J_Q . The approximations (70)–(72) then yield all the components of \mathbf{S} . The only remaining task is the solution of six scalar transfer equations with known source functions.

When $\varphi_B \neq 0$, the coefficients $M_{2\alpha}$ in (70)–(72) should be replaced by the coefficients $H_{2\alpha}$. This amounts to making the changes,

$$M_{23} \rightarrow (c_1 M_{23} + s_1 M_{24}), \quad M_{24} \rightarrow (c_1 M_{24} - s_1 M_{23}), \quad (85)$$

$$M_{25} \rightarrow (c_2 M_{25} - s_2 M_{26}), \quad M_{26} \rightarrow (c_2 M_{26} + s_2 M_{25}), \quad (86)$$

where the c_i and s_i , $i = 1, 2$ are defined in Eqs. (43) and (44).

In Fig. 16 we compare polarization diagrams obtained with this approximation and with a full PALI-H iterative method. It is clear that the differences fall within the error bars of a standard measurement. The calculation of the approximate solution is a factor of 10 faster than the full PALI-H code. It is so fast that one can think of using it as part of an inversion code to set up estimates of the vector magnetic field.

For the purpose of estimating the magnetic field, it is possible to use an even cruder version of the above approximation, already suggested in FS91. The components J_I and J_Q and the components of \mathbf{S} are calculated as above. The surface polarization is then estimated with the Eddington-Barbier approximation, $\mathbf{I}(0, x, \mu) \simeq \mathbf{S}(\tau_x)$, with $\tau_x \simeq \mu/\phi(x)$. For $\varphi_B = 0$ and ϵ negligible compared to unity, this approximation yields for the surface value of the Stokes parameters :

$$I(x, \mu, \varphi) \simeq J_I(\tau_x) + S_I^*(\tau_x), \quad (87)$$

$$Q(x, \mu, \varphi) \simeq \left\{ \frac{\sqrt{W}}{2\sqrt{2}} 3(1 - \mu^2) M_{22} + \sqrt{3W} \mu \sqrt{1 - \mu^2} [M_{23} \cos \varphi - M_{24} \sin \varphi] - \frac{\sqrt{3W}}{2} (1 + \mu^2) [M_{25} \cos 2\varphi + M_{26} \sin 2\varphi] \right\} J_Q(\tau_x), \quad (88)$$

$$U(x, \mu, \varphi) \simeq \left\{ -\sqrt{3W} \sqrt{1 - \mu^2} [M_{24} \cos \varphi + M_{23} \sin \varphi] + \sqrt{3W} \mu [M_{26} \cos 2\varphi - M_{25} \sin 2\varphi] \right\} J_Q(\tau_x). \quad (89)$$

An approximation for the three components of the Stokes source vector constructed with the same method is given in FS91 (it contains however some misprints).

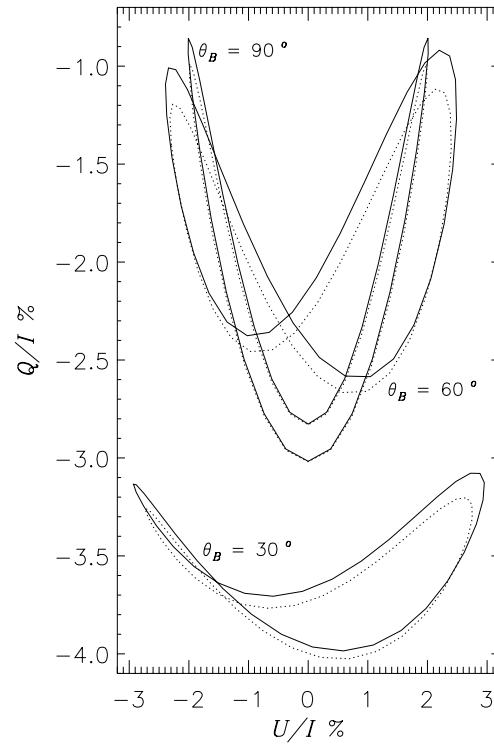


Fig. 16. Polarization diagrams showing the relative accuracy of the approximation defined in Sect. 5.3. Same atmospheric model as in Fig. 11 with magnetic field parameters $(\gamma_B, \varphi_B) = (1, 0^\circ)$ and different values of θ_B . The diagrams refer to line centre and the LOS co-latitude $\theta = 87^\circ$. The solid lines show the results of full PALI-H computations, and the dotted lines the approximate solutions. The relative errors are 20 %, or less

7. Concluding remarks

The Approximate Lambda Iteration method presented in this paper, has several advantages over the perturbation method introduced in FS91. Since it is an operator perturbation method, it does not explicitly make use of the smallness of the degree of polarization and is able to handle situations where the polarization is arbitrarily large. Also the speed of convergence is entirely independent of the vector magnetic field. By using a Fourier decomposition with respect to φ instead of $\Delta\varphi = \varphi - \varphi_B$, it offers the possibility to calculate the Hanle effect produced by a magnetic field with a depth-dependent co-latitude, strength and also azimuthal angle. The numerical accuracy of the PALI-H method is also somewhat superior to that of the FS91 perturbation method. It is accurate up to the 6th significant digit, when compared to a direct numerical solution obtained by a Feautrier method. The main advantage is the gain in CPU time, as the PALI-H method is 50 times faster than Feautrier method for most of the practical problems of interest in Solar Physics.

Introducing an irreducible radiation field, we are able to write a six-component vector radiative transfer equation with a vector source function depending only on the optical depth and we could thus give a very simple derivation, significantly sim-

pler than in FS91, of the integral equation which is the starting point for the PALI-H method.

It should be stressed that the perturbation method developed in FS91 can handle both complete and partial frequency redistribution problems whereas here only complete frequency redistribution has been considered. A few preliminary tests have shown that the PALI-H method can be adapted to partial frequency redistribution. That such a generalization is feasible has already been shown for resonance polarization in zero magnetic field by Paletou & Faurobert-Scholl (1997).

It is needless to say that the PALI-H method can handle any radiative transfer problems involving a non-axisymmetric radiation field, as for example the scattering of a non-axisymmetric incident radiation field in a non-magnetic atmosphere. In this case \hat{H}_B reduces to the (6×6) identity matrix.

Here the PALI-H method has been presented and applied with the assumption that the absorption profile ϕ is independent of optical depth. It works equally well for real atmospheres where this assumption would not be correct. The depth dependence of the profile need only to be taken into account when calculating the formal solution of the transfer equation (50) and the mean irreducible intensity $J(\tau)$ with the expression given in Eq. (49). Naturally, when ϕ is depth-dependent, the kernel \hat{K} of the integral equation (51) depends separately on both the arguments τ and τ' , but the iterative method never makes explicitly use of this equation.

Considering the inherent uncertainties in the observed data, the simple perturbative approximation for the Hanle effect introduced in this paper should prove very useful for preliminary analyses. This approximation enables one to reduce the six-dimensional vector transfer problem for the irreducible radiation field into a two-dimensional modified resonance polarization problem which yields the azimuthal average of the irreducible radiation field. The azimuth dependent components can then be calculated by solving four scalar transfer problems with known source functions or simply by using an Eddington-Barbier approximation, when only the surface polarization is of interest.

Acknowledgements. K.N.N. would like to thank the staff members of Observatoire de Nice, for their warm hospitality during the course of this work. A travel grant from IAU Comm. 38 and a grant from the French MENRT enabled him to visit the Observatoire de la Côte d'Azur in 1996 and 1997. This support is gratefully acknowledged. The authors have benefitted from stimulating discussions with Drs. V. Bommier, E. Landi Degl'Innocenti, F. Paletou and J. O. Stenflo.

References

- Auer L.H., Fabiani Bendicho P., Trujillo-Bueno J., 1994, A&A 292, 599
 Bommier V., 1996, in *Solar Polarization*, Stenflo J.O., Nagendra K.N. (eds), Kluwer Academic Publishers, Dordrecht, p. 29 (see also Solar Phys. 164, 29)
 Bommier V., Landi Degl'Innocenti E., Sahal-Brechot, S., 1989, A&A 211, 230
 Bommier V., Landi Degl'Innocenti E., Sahal-Brechot, S., 1991, A&A 244, 383

- Chandrasekhar S., 1960, *Radiative Transfer*, Dover, New York
 Domke H., 1971, SvA 15, 266
 Faurobert M., 1987, A&A 178, 269
 Faurobert-Scholl M., 1991, A&A 246, 469 (FS91)
 Faurobert-Scholl M., 1993, *Polarisation de Résonance des Raies Spectrales et effet Hanle*, Notice de Travaux, Publication de l'Observatoire de la Côte d'Azur.
 Faurobert-Scholl M., 1996, in *Solar Polarization*, Stenflo J.O., Nagendra K.N. (eds), Kluwer Academic Publishers, Dordrecht, p. 79 (see also Solar Phys. 164, 79)
 Faurobert-Scholl M., Frisch H., Nagendra K.N., 1997, A&A 322, 896 (Paper I)
 Frisch H., 1988, in *Radiation in Moving Gaseous Media*, 18th Advanced Course, Swiss Society of Astronomy and Astrophysics, Chmielewsky Y., Lanz T. (eds), Publication de l'Observatoire de Genève, p. 339
 Ignace R., Nordsiek K.H., Cassinelli J.P., 1997, The Hanle Effect as a Diagnostic of Magnetic Fields in Stellar Envelopes I. Theoretical Results for Integrated Line Profiles, preprint
 Ivanov V.V., 1995, A&A 303, 609
 Ivanov V.V., Grachev S.I., Loskutov V.M., 1997, A&A 318, 315
 Landi Degl'Innocenti E., 1984, Solar Phys. 91, 1
 Landi Degl'Innocenti E., 1985, Solar Phys. 102, 1
 Landi Degl'Innocenti E., Bommier, V., Sahal-Brechot, S., 1987, A&A 186, 335
 Landi Degl'Innocenti E., Bommier, V., Sahal-Brechot, S., 1990, A&A 235, 459
 Landi Degl'Innocenti M., Landi Degl'Innocenti E., 1988, A&A 192, 374
 Paletou F., Faurobert-Scholl M., 1997, A&A 328, 343
 Stenflo J.O., 1994, *Solar Magnetic Fields—Polarized Radiation Diagnostics*, Kluwer, Dordrecht